Simultaneous Multiresolution Imaging Based on Multimode MIMO-SAR

Fang Zhou, *Member, IEEE*, Guoqing Shen, Yifan Liu, Jing Fang, Jiajia Zhang, and Mengdao Xing, *Fellow, IEEE*

***Abstract*—This article proposes a novel imaging mode which allows for the acquisition of SAR images with different resolution in a single imaging process, specifically designed for multiple-input–multiple-output synthetic aperture radar (MIMO-SAR). To achieve this, a multimode array system model based on 2-D intrapulse scanning is established, followed by the division of full aperture signals into subaperture signals. Improved azimuth phase coding (APC) technology is then employed to separate multimode echo signals, and spatial filtering technology and range digital beam forming technology are used to remove ambiguity in azimuth and range of the subaperture signals of each mode. Finally, subaperture image coherent fusion algorithm is used to generate high-resolution images corresponding to the full aperture of each mode. Simulation results show that the improved APC can effectively separate multimode echo signals, and the multiresolution characteristics and imaging effect are verified.**

***Index Terms*—Azimuth phase coding (APC), multimode, multiple-input–multiple-output synthetic aperture radar (MIMO-SAR), multiresolution, subaperture.**

I. Introduction

MULTIPLE-INPUT–MULTIPLE-OUTPUT synthetic aperture radar (MIMO-SAR) can obtain microwave images with high resolution wide swath (HRWS) due to its all-day and all-weather capability, which is widely used in military and civilian fields and will be the key development direction of spaceborne SAR in the future [1], [2], [3], [4], [5], [6]. However, due to the limitation of the minimum antenna area, the high resolution of spaceborne SAR and the large mapping belt form a contradiction [7], [8]. In order to solve this contradiction, scholars at home and abroad have conducted a lot of research [9], [10], [11], [12], [13], [14]. In [9], a large antenna is divided along the pitching direction, and the range ambiguity is solved by using the range digital beam forming (DBF) technology to obtain a wide-swath along the range. By contrast with it, the large antenna is segmented along the course to obtain a wide-swath along the course under the condition of low pulse repetition frequency (PRF), as is proposed in [10], [11], [12]. And their common disadvantages are a small transmission area for antenna and a low signal-to-noise (SNR) ratio for echo. A new method in [13] proposes a high-resolution wide swath imaging model for pitching dimensional intrapulse scanning under the condition of low PRF, and uses an array to receive the echo. Then the imaging results of high-resolution wide-swath can be obtained by solving the ambiguity in azimuth and range with 2-D degrees of freedom. However, the transmission channel utilization of this model is low. By contrast with it, a high-resolution wide-swath imaging model based on range-azimuth 2-D intrapulse scanning, under the condition of low PRF, is proposed in [14]. With using full aperture array to transmit and receive, the imaging results of high-resolution wide-swath can be obtained by solving ambiguity in azimuth and range with 2-D degrees of freedom, which fully improves the utilization of the transmission channel. However, this model cannot obtain SAR images with different resolution in a single imaging processing, and the data volume of the radar imaging processing system is too large. If the radar lacks the capability of simultaneous multimode imaging, detailed observations must be completed through multiple flights, which may not be feasible in practical applications. Therefore, it is of great significance for a modern radar to possess the capability of multiple mode SAR [15], [16], which enables obtaining a coarse resolution SAR image of an entire imaging area while capturing details of specific areas. On the basic of the multidimensional waveform coding, DBF technology is capable to simultaneously form the beam orientation of the multiple mode, which can enhance the imaging flexibility of SAR system. Finally, after separating the echo of different modes, the SAR images of the global coarse resolution and local high fine resolution can be simultaneously obtained through a single flight. Krieger et al. [17] only provided a simple example of multimode imaging and does not elaborate on the operational mode and specific implementation process of multimode SAR imaging in detail. Although some multimode imaging models that divide the large antenna along the course have been proposed in [18], [19],

Manuscript received 13 April 2023; revised 31 May 2023, 6 July 2023, and 25 July 2023; accepted 4 August 2023. Date of publication 15 August 2023; date of current version 20 September 2023. This work was supported in part by the Natural Science Foundation of Anhui Province under Grant 2208085MF156, in part by the Fundamental Research Funds for the Central Universities under Grant JZ2022HGTB0329, and in part by the Aeronautical Science Foundation of China under Grant 2019200P4001. *(Corresponding author: Jiajia Zhang.)*

Fang Zhou, Guoqing Shen, Yifan Liu, and Jing Fang are with the School of Computer Science and Information Engineering and the Intelligent Interconnected Systems Laboratory of Anhui Province, Hefei University of Technology, Hefei 230009, China (e-mail: zhoufang@hfut.edu.cn; hfutsgq@mail.hfut.edu.cn; yifan19981203@163.com; fangjing@hfut.edu.cn).

Jiajia Zhang is with the Key Laboratory of Aperture Array and Space Application, East China Research Institute of Electronic Engineering, Hefei 230088, China (e-mail: zjjreal@126.com).

Mengdao Xing is with the National Laboratory of Radar Signal Processing, Xidian University, Xi'an 710071, China, and also with the Academy of Advanced Interdisciplinary Research, Xidian University, Xi'an 710071, China (e-mail: xmd@xidian.edu.cn).

Digital Object Identifier 10.1109/JSTARS.2023.3305234

[20], and [21], there are common shortcomings, such as low resolution, small antenna transmission area, and low echo SNR ratio. Therefore, it is of great significance to study multimode imaging.

Multimode imaging system is the main means for SAR to obtain different high-resolution target images, and how to separate the received echoes of each mode is the key to study this imaging system. At present, two types of echo separation methods are widely used: band pass filter (BPF) method [22], [23] and azimuth phase coding (APC) method [24], [25], [26], [27], [28]. The BPF method is based on the premise that each mode has a different carrier frequency, and the echo signals of each mode are separated by BPFs with different center frequencies at the receiving end. However, due to the limited frequency band range, it is sometimes impossible to use the frequency division mode for all modes. Therefore, some works introduce APC to separate multimode echo signals of the same carrier frequency, but the separation condition is in the absence of orientation ambiguity, which limits the limitations of echo separation. Simultaneously, the amount of data generated by spaceborne SAR is so large that it brings difficulties to the real-time transmission and storage of data. Therefore, how to reduce the storage pressure and imaging load of multichannel satellites is another key to studying in this imaging system. A method that proposes fast factored back projection (FFBP) algorithm is proposed in [29] and [30], which images each subaperture data in a local polar coordinate system. However, during image fusion, the error caused by 2-D interpolation reduces the imaging quality. And there is an article that proposes an algorithm which will generate grating lobe [31] due to the overlap between subapertures, thus reducing the imaging efficiency [32].

In view of the above problems, this article proposes a simultaneous multiresolution imaging mode based on multimode MIMO-SAR. In range, high resolution wide-swath images in range are obtained by transmitting step frequency signals and removing ambiguous. In azimuth, high-resolution wide-swath images in azimuth are obtained through coherent fusion of low pulse repetition rate and subaperture image [33], [34], [35], [36]. Meanwhile, the improved APC technology is used to separate multimode echo signals. Therefore, on one hand, this imaging mode meets the requirements of high-resolution wide-swath imaging, on the other hand, it realizes the requirements of obtaining SAR images with different resolution in single imaging processing.

II. MIMO-SAR System Working Model

The imaging mode of the MIMO-SAR system adopts a 2-D intrapulse scanning method. That is to say: First, the system transmits multiple subpulses in a pulse transmission time. Then, the range–azimuth 2-D narrow beam is formed by using the whole array antenna. Finally, the phase weighting technique is used to control the beam to scan different range–azimuth subswaths in different subpulse times. Take the example of a $2*3$ transceiver array. At the transmitter, DBF technology is used to simultaneously form the beam orientation of the stripe mode and the spotlight mode. Then, the two modes control the pitching beam to scan two pitching swaths from far to near. And each

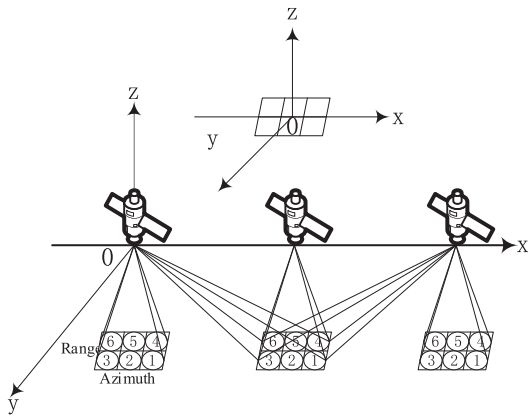

Fig. 1. Multimode MIMO-SAR transceiver model.

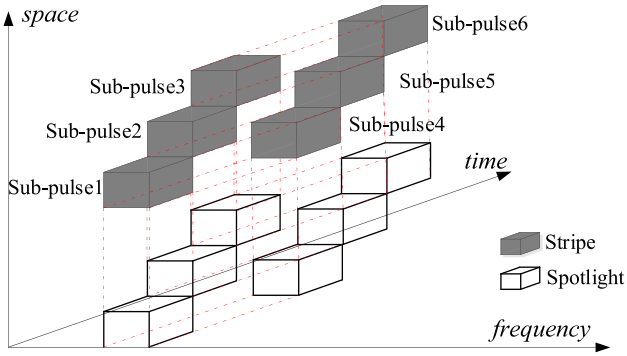

Fig. 2. Operational principle of Fig. 1 in a transmitting pulse time.

pitching swath uses three beams in azimuth to scan from front to back in-flight direction, forming three sub scenes in azimuth. The scanning sequence of each sub scene is shown in Fig. 1.

The operational principle of multimode MIMO-SAR model in a transmitting pulse time is depicted in Fig. 2. The hollow cuboid represents the spotlight signal, while the solid cuboid denotes the stripe signal. The system transmits six subpulses in a transmitting pulse time, and each cuboid denotes the system transmits a subpulse signal of each mode within a transmitting subpulse time. At the transmitting end, DBF technology is used to simultaneously form the beam orientation of the stripe mode and the spotlight mode, resulting in the spatial separation of the signals of the two operational modes in a single transmitting pulse time. Meanwhile, because the signal of each imaging mode adopts the form of time-sharing transmitting subpulse, the subpulse signals of each mode are temporally separated. Finally, after obtaining and separating the echo of two modes, the global coarse resolution and local high fine resolution SAR images can be simultaneously obtained through a single flight, which can achieve the simultaneous multiresolution imaging.

III. Related Works and Signal Model

A. Principle of Subaperture Division

The frequency domain representation of the echo signal is shown in Fig. 3. B_a is the full aperture of scene Doppler bandwidth and B_{inst} is the instantaneous Doppler bandwidth. The edge real oblique line represents the time-frequency relationship

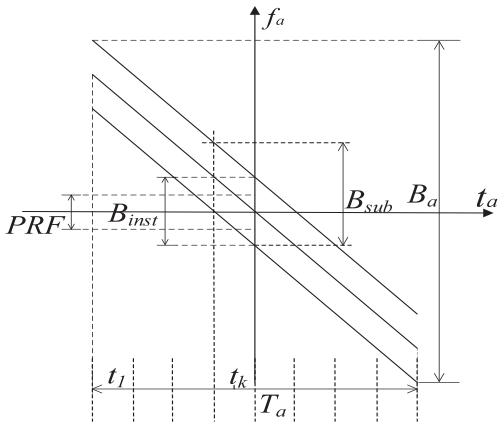

Fig. 3. Time frequency diagram of single equivalent phase center.

of the edge point of the scene, and the middle real oblique line represents the time-frequency relationship of the scene center. Therefore, B_a can be expressed as

$$B_a = -K_a T_a + B_{\text{inst}} \tag{1}$$

where $K_a = -2v^2 f_c/(cR)$ is the Doppler frequency modulation and T_a is the synthetic aperture time.

To remove the Doppler ambiguity of the full aperture signal, the PRF needs to meet the condition expressed as

$$F_{\text{PRF}} \geq B_a/Q \tag{2}$$

where Q is an ambiguity number and F_{PRF} denotes the required PRF in removing the ambiguity of full aperture signal.

If the full aperture signal is divided into *K*-segment, the scene Doppler bandwidth of the *k*-segment subaperture signal [37] can be expressed as

$$B_{\text{sub}} \approx -K_a T_{\text{sub}} + B_{\text{inst}} + K_a t_k \tag{3}$$

where $T_{\text{sub}=} T_a/K$ is the synthetic aperture time of subaperture and $t_k (k = 1, 2, \ldots, K)$ denotes the center time of the azimuth time corresponding to the *k*-segment subaperture. And the third item in (3) shows that the Doppler shift of the *k*-segment subaperture signal of each equivalent phase center takes $K_a t_k$ as the center, resulting in different Doppler centers of each subaperture signal.

To remove the Doppler ambiguity of the subaperture signal, the PRF needs to meet the condition expressed as

$$f_{\text{PRF}} \geq \frac{B_{\text{sub}}}{Q} \tag{4}$$

where Q is an ambiguity number and f_{PRF} denotes the required PRF in removing the ambiguity of subaperture signal.

By comparing (2) and (4), it can be seen that PRF of subaperture processing is B_a/B_{sub} times smaller than the full aperture, which can greatly reduce the amount of data of the imaging system.

B. Improved Azimuth Phase Coding

For receiving and transmitting modes of the configuration, it is assumed that the large array antenna of the system is

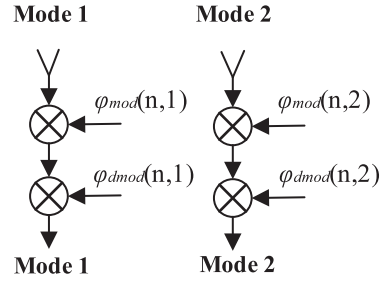

Fig. 4. Process of modulation and demodulation of the multimode azimuth phase.

divided into $U \times V$ subapertures. That is, there are U antenna subapertures in the pitching dimension, and the size of each antenna subaperture is D_r. There are V antenna subapertures in the azimuth dimension, and the size of each antenna subaperture is D_a. Assuming that the center coordinate of the subaperture of the array antenna in row 1 and column 1 is (X_1, Y_1, Z), and then the center coordinate of the subaperture of the array antenna in row $u (u = 1, 2, \ldots, U)$ and column $v (v = 1, 2, \ldots, V)$ is (X_v, Y_u, Z), where $X_v = X_1 + (v-1)D_a, Y_u = Y_1 + (u-1)D_r$. Therefore, the phase center of the transmitting beam is the center of the antenna array, that is $((X_V + X_1)/2, (Y_U + Y_1)/2, Z)$. According to the principle of equivalent phase center, the equivalent phase center position of the receiving beam is (X'_v, Y'_u, Z), where

$$X'_v = \frac{X_{\text{transmit}} + X_{\text{receive}}}{2} = \frac{X_v}{2} + \frac{X_1 + X_V}{4} \tag{5}$$

$$Y'_u = \frac{Y_{\text{transmit}} + Y_{\text{receive}}}{2} = \frac{Y_u}{2} + \frac{Y_1 + Y_U}{4}. \tag{6}$$

After designing the receiving and transmitting modes, this article uses the azimuth phase encoding technology to separate the multimode echo signals. The system is capable of utilizing multiple channels to receive echoes in azimuth, allowing for a single transmitter and multiple receivers. This enables each altitude dimension's equivalent phase center to possess multiple degrees of freedom in azimuth, which can be utilized for spatial filtering. However, since the process of modulation and demodulation of the original azimuth phase encoding technology will generate additional residual phase, the signal needs to be transformed to the slow time domain before it can be compensated. This process is cumbersome and the calculation process is complex. This article outlines an improvement to azimuth phase encoding technology which eliminates the need for compensating residual phase after demodulation. The process of modulation and demodulation of the multimode azimuth phase is shown in Fig. 4.

For the APC, the encoding phase and decoding phase are improved as follows. First, the azimuth phase encoding phase of the *p*th SAR mode can be expressed as

$$\varphi_{\text{mod}}(n, p) = -\frac{2\pi n}{P}(n - p). \tag{7}$$

Second, the azimuth phase decoding phase of the *p*th SAR mode can be expressed as

$$\varphi_{\text{dmod}}(n,p)=\frac{2\pi n}{P}(n-1) \tag{8}$$

where *n* denotes the number of transmitting pulses and *P* denotes the number of SAR modes.

Since the echo received by each receiving channel is the linear superposition of the corresponding echo of each SAR mode, the residual modulation phase of the echo of mode *p* is

$$\begin{aligned}\varphi_{\text{res}}(n,p)&=\varphi_{\text{mod}}(n,p)+\varphi_{\text{dmod}}(n,p)\\&=-\frac{2\pi n}{P}(n-p)+\frac{2\pi n}{P}(n-1)\\&=\frac{2\pi(p-1)f'_a}{P}t_a\end{aligned} \tag{9}$$

where $t_a=n/f'_a$ denotes the slow time in azimuth and f'_a denotes the PRF.

Equation (9) is expressed as frequency shift in the azimuth frequency domain. Therefore, the Doppler frequency shift corresponding to the *p*th SAR mode echo can be expressed as

$$\Delta f_d(p)=\frac{(p-1)f'_a}{P}. \tag{10}$$

C. Received Signal Model

Based on Section II, we assume that the system has *N* pitching submapping zones and each pitching submapping zone has *M* subbeams in azimuth. At the same time, the width of subbeam pulses in the same pitching submapping zone is the same, while the width of subbeam pulses in different pitching submapping zones may be different. If the spotlight mode and the stripe mode have a scattering point $P_{n,\text{spotlight}}$ $(X_{n,\text{spotlight}},Y_{n,\text{spotlight}},Z_{n,\text{spotlight}})$ and $P_{n,\text{stripe}}(X_{n,\text{stripe}}\,Y_{n,\text{stripe}},Z_{n,\text{stripe}})$, respectively, in the *n*th pitching sub mapping zone. With the progress of SAR beam observation, the range of time and angle in azimuth of point target $P_{n,\text{spotlight}}$and $P_{n,\text{stripe}}$ illuminated by the *m*th azimuth sub beam are $T_{\text{beam},m,\text{spotlight}}$, $\varphi_{\text{beam},m,\text{spotlight}}$, and $T_{\text{beam},m,\text{stripe}}$, $\varphi_{\text{beam},m\ \text{stripe}}$, respectively.

Based on Section III-A and III-B, the full aperture signal is now divided into *K*-segments. Then the range of time in azimuth of the *k*th subaperture signal can be expressed as

$$t_a\in\left[-\frac{T_a}{2K}:\frac{T_a}{2K}\right]+t_k=t_{\text{sub}}+t_k. \tag{11}$$

In the receiver, the baseband signal of the *k*th subaperture received by the subaperture of the array antenna in row *u* and column *v* can be expressed as

$$\begin{aligned}S_{uv,k}(t_r,t_{\text{sub}},t_k)&=S_{uv,k,\text{spotlight}}(t_r,t_{\text{sub}},t_k)\\&\times\exp([\varphi_{\text{mod}}(n,1)+\varphi_{\text{dmod}}(n,1)])\\&+S_{uv,k,\text{stripe}}(t_r,t_{\text{sub}},t_k)\times\exp([\varphi_{\text{mod}}(n,2)\\&+\varphi_{\text{dmod}}(n,2)])\\S_{uv,k,\text{spotlight}}(t_r,t_{\text{sub}},t_k)&\times\exp[\varphi_{\text{res}}(n,1)]\\&+S_{uv,k,\text{stripe}}(t_r,t_{\text{sub}},t_k)\times\exp[\varphi_{\text{res}}(n,2)]\end{aligned} \tag{12}$$

where

$$\begin{aligned}S_{uv,k,\Delta}(t_r,t_{\text{sub}},t_k)&=a_{r,k,\Delta}(t_r)\times a_{a,k,\Delta}(t_{\text{sub}}+t_k)\\&\times\exp\left[\begin{array}{c}-j2\pi f_c\left(\Delta T_{(m,n)}(t_{\text{sub}}+t_k)\right.\\\left.+\frac{2R_{uv,k,n,\Delta}(t_{\text{sub}}+t_k)}{c}\right)\end{array}\right]\\&\times\exp\left[\begin{array}{c}j\pi\gamma\left(t_r-\Delta T_{(m,n)}(t_{\text{sub}}+t_k)\right.\\\left.-\frac{2R_{uv,k,n,\Delta}(t_{\text{sub}}+t_k)}{c}\right)\end{array}\right]\\&\times\exp\left(j\frac{2\pi f_a}{v}X'_{uv}\right)\\\Delta&\in\{\text{spotlight},\text{stripe}\}\end{aligned} \tag{13}$$

where $a_{r,k,\Delta}(t_r)=\text{rect}[(t_r-\frac{2R_{uv,k,n,\Delta}(t_{\text{sub}}+t_k)}{c}-\Delta T_{(m,n)}(t_{\text{sub}}+t_k))T_p(m,n)]$, $\Delta\in\{\text{spotlight},\text{stripe}\}$ denotes the range envelope function. $a_{a,k,\Delta}\ (t_{\text{sub}}+t_k)=\text{rect}[(v(t_{\text{sub}}+t_k)+X'_v-X_{n,\Delta})/L_a],\Delta\in\{\text{spotlight},\text{stripe}\}$ denotes the azimuth envelope function. t_r denotes fast time. t_{sub} denotes slow time. v denotes radar speed. L_a denotes synthetic aperture length. f_c denotes carrier frequency. γ denotes frequency modulation. $\Delta T_{(m,n)}(t_{\text{sub}}+t_k)=\sum_{i=1}^{n-1}MT_p(m,n)+(m-1)T_p(m,n)$ is the transmitting delay of the *k*th subaperture signal of the *m*th azimuth sub beam in the *n*th pitching sub mapping zone, and the transmitting delay is independent of t_{sub}, which does not affect the delayed imaging of each subaperture. $R_{uv,k,n,\Delta}(t_{\text{sub}}+t_k)=[(X'_v-X_{n,\Delta}+v(t_{\text{sub}}+t_k))^2+(Y'_u-Y_{n,\Delta})^2+(Z-Z_{n,\Delta})^2]^{1/2},\Delta\in\{\text{spotlight},\text{stripe}\}$ denotes the instantaneous slant distance corresponding to the *k*th segment subaperture signal. It is assumed that the ground undulation is not taken into account, and it can be expressed as $R_{uv,k,n,\Delta}(t_{\text{sub}}+t_k)\approx Y'_u\cdot\sin\theta_{n,\Delta}+R_{k,n,\Delta}(t_{\text{sub}}+t_k)$, $\Delta\in\{\text{spotlight},\text{stripe}\}$, where $\theta_{n,\Delta},\Delta\in\{\text{spottlight},\text{stripe}\}$ is the perspective of point target $P_{n,\Delta},\Delta\in\{\text{spotlight},\text{stripe}\}$. $f_a(-f_{\text{PRF}}\le f_a\le f_{\text{PRF}})$ denotes the Doppler frequency of the subaperture signal. The additional modulation phase can be written as $\exp(j2\pi f_aX'_{uv}/v)$, which does not change the frequency modulation characteristics of the signal.

IV. High-Resolution Wide-Swath Imaging Processing

Before obtaining the high-resolution images of each mode signal, it is necessary to separate the echo signals of each mode and reconstruct the subaperture signals with no ambiguity in the azimuth and range of each mode. The signal processing flow chart is shown in Fig. 5.

A. Echo Separation of Multimode Signal Based on Improved Azimuth Phase Coding

Based on the analysis presented in Section III-B, the traditional APC can demodulate the azimuth phase of each mode signal without azimuth ambiguity. It is achieved by utilizing spatial filtering technology to separate the signal of each mode and then transforming the data of each mode from the $f_a$domain

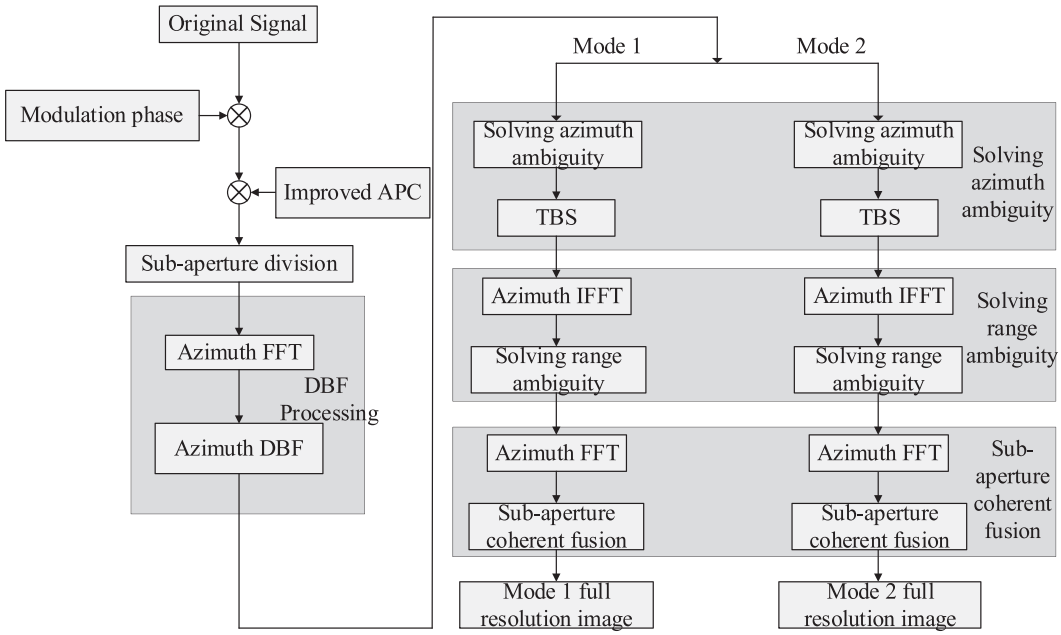

Fig. 5. Signal processing flow chart.

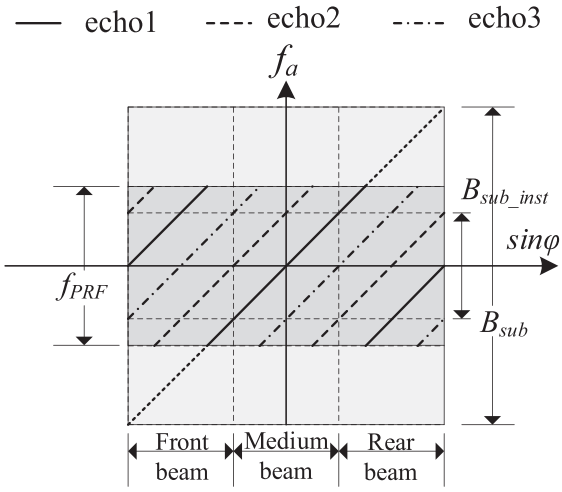

Fig. 6. Sketch of the angle-Doppler relation.

to the t_{sub} domain to compensate for residual phase. However, the traditional APC is no longer applicable in this imaging mode. After adding a modulation phase to the original signal in this article, the improved APC is used to achieve echo separation. Fig. 6 shows the sketch of the angle-Doppler relation of the received signal of the improved APC waveforms.

In domain f_a, the corresponding relationship between azimuth squint angle θ and azimuth frequency f_a can be represented as

$$f_a = \frac{2v}{\lambda}\sin\theta. \tag{14}$$

Due to the Doppler frequency shift generated by the azimuth phase encoding, the relationship between squint angle in azimuth and frequency in azimuth of echoes in different modes is inconsistent, as shown in Fig. 6. Therefore, the relationship between θ_p and f_a of echo p can be written as

$$\sin\theta_p = \frac{\lambda}{2v}\left[f_a - \Delta f_d(p)\right]. \tag{15}$$

According to the corresponding relationship of (15), different echoes can be separated in angle. However, the PRF is considered slightly larger than the Nyquist sampling rate, the Doppler spectra of the demodulated APC waveform echoes in the Doppler domain is aliasing. In view of this situation, (15) is revised as

$$\sin\theta_p = \frac{\lambda}{2v}\left[f_a - \Delta f_d(p) + M_p f_{\text{PRF}}\right] \tag{16}$$

where M_p denotes the ambiguity number of azimuth spectrum of echo p within a certain azimuth frequency range.

On the basis of the above separation principle, the process of echo separation of multimode is as follows. In row u, the array vector of P ($P = U$) channels in azimuth composed of the kth subaperture signal received by any P array antenna subaperture can be shown as

$$\boldsymbol{\beta}(\theta_p, u) = \left[\exp\left(j\frac{4\pi}{\lambda}X'_{uP_1}\sin\theta_p\right), \ldots, \exp\left(j\frac{4\pi}{\lambda}X'_{uP_p}\sin\theta_p\right)\right]^T_{P\times 1} \tag{17}$$

where T is the matrix transpose, $P_1(1 \le P_1 < 3)$,$P_p(1 < P_p \le 3)$, and $P_1 \le P_p$.

Then the array vector matrix can be constructed as

$$\mathbf{B}(\theta_p, u) = \left[\boldsymbol{\beta}(\theta_1, u), \ldots, \boldsymbol{\beta}(\theta_p, u), \ldots, \boldsymbol{\beta}(\theta_P, u)\right]_{P\times P}. \tag{18}$$

The weight vector is

$$\mathbf{W}(\theta_p, u) = \mathbf{B}^{+}(\theta_p, u)\mathbf{e}_p \tag{19}$$

where $+$ represents the pseudo inverse of the matrix and $e_p = [e_1, \ldots, e_q, \ldots, e_P]^T$ $e_{q=p} = 1$, and $e_{q\neq p} = 0$.

Finally, in row u, the matrix of the P receiving echoes of the kth subaperture signal can be extracted as

$$\mathbf{S}_{u,k}(t_r, f_a) = [S_{uP_1,k}(t_r, f_a), \ldots, S_{uP_p,k}(t_r, f_a)]_{1\times P}. \quad (20)$$

Multiplying (19) by (20), the separated echo signal of multimode can be obtained as

$$\begin{aligned} S_{u,v,k,\Delta}(t_r, f_a) = \sum_{n=1}^{N}\sum_{m=1}^{M} & W_{a,k,\Delta}(f_a + f_{dc}) \times \exp(j2\pi f_a t_k) \times \\ & \exp\left[-j2\pi(f_a + f_{dc})X_{n,\Delta}/v\right] \times \\ & \exp\left[\begin{matrix} -j2\pi \\ \times \frac{R_{k,B,n,\Delta}\sqrt{f_{aM}^2 - (f_a+f_{dc})^2}}{v} \end{matrix}\right] \times \\ & w_{r,k,\Delta}(t_r) \times \exp(-j4\pi {Y'}_u \sin\theta_{n,\Delta}/\lambda) \times \\ & \exp(j4\pi {X'}_v \sin\varphi_{m,\Delta}/\lambda), \\ & \Delta \in \{\text{spotlight}, \text{stripe}\} \end{aligned} \quad (21)$$

where $w_{r,k,\Delta}(t_r) = \text{sinc}(t_r - \Delta T_n(\varphi_{k,m,\Delta}) - 2R_{k,B,n,\Delta}(f_a + f_{dc}) \times \frac{\cos\varphi_{k,m,\Delta}}{c}), \Delta \in \{\text{spotlight}, \text{stripe}\}$ is the time domain window function in range. $W_{a,k,\Delta}(\cdot), \Delta \in \{\text{spotlight}, \text{stripe}\}$ denotes the azimuth frequency domain window function. $R_{k,B,n,\Delta} = (Y_{n,\Delta}^2 + (Z - Z_{n,\Delta})^2)^{1/2}$ $\Delta \in \{\text{spotlight}, \text{stripe}\}$ is the shortest slant distance from radar to point target $P_{n,\Delta}, \Delta \in \{\text{spotlight}, \text{stripe}\}$. $\Delta T_n(\varphi_{k,m,\Delta}), \Delta \in \{\text{spotlight}, \text{stripe}\}$ is the signal transmission delay at angles $\varphi_{k,m,\Delta}, \Delta \in \{\text{spotlight}, \text{stripe}\}$. $\varphi_{k,m,\Delta} \in \varphi_{\text{beam},m,\Delta}, m = 1, 2, \ldots, M$, $\Delta \in \{\text{spotlight}, \text{stripe}\}$, $\Delta T_n\ (\varphi_{k,m,\nabla}) = \sum_{i=1}^{n-1} VT_p(m,n) + (m-1)T_p(m,n), \nabla \in \{\text{spotlight}, \text{stripe}\}$, $f_{aM} = 2v/\lambda$.

B. Restoration of Unambiguous Signal in Azimuth Based on Spatial Filtering

After echo signals of the multimode are separated, the analysis of the signals shows that the echoes illuminated by sub beams in different directions correspond to different Doppler frequency bands. As the number of subapertures varies, different subaperture region may have multiple Doppler frequency bands, but with different Doppler frequency bands there exist distance misalignment. Therefore, all possible Doppler frequency bands in the subaperture area constitute the complete azimuth spectrum of the subaperture signal. Then according to (4), since the azimuth sampling of the subaperture is $f_{\text{PRF}} \geq B_{\text{sub}}/M$, the azimuth spectrum will be aliased. The schematic diagram of ambiguity in azimuth is shown in Fig. 7. At the same time, although range misalignment may occur between multiple Doppler bands in the subaperture area, it will not affect the azimuth ambiguity of subaperture. After the signal is transformed into Doppler domain, the unambiguous signal in azimuth can be recovered by filtering the same subaperture signal of each mode with the weight vector.

According to Section III-A, the Doppler center of the kth subaperture signal is $f_{dc} = K_a\, t_k$. Therefore, the Doppler center

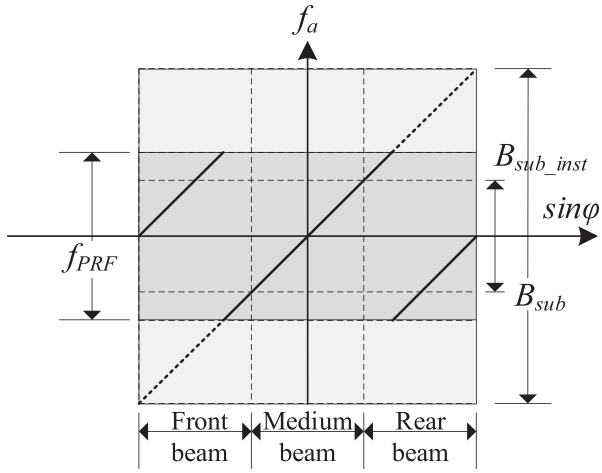

Fig. 7. Schematic diagram in azimuth ambiguity.

compensation function can be constructed as

$$H = \exp\left[-j2\pi f_{dc}(t_{\text{sub}} + t_k)\right]. \quad (22)$$

Multiplying (21) by (22), the signal of the kth subaperture can be rewritten as

$$\begin{aligned} S_{u,v,k,\Delta}(t_r, t_{\text{sub}}, t_k) &= S_{u,v,k,\Delta}(t_r, t_{\text{sub}}, t_k)H, \\ &\Delta \in \{\text{spotlight}, \text{stripe}\}. \end{aligned} \quad (23)$$

The ambiguity in azimuth can be removed only when the freedom in azimuth degree is not less than the number in azimuth ambiguity. The process of removing ambiguity in azimuth is as follows. For the kth segment subaperture signal received by the uth row array antenna, the array vector of V channels in azimuth can be written as

$$\begin{aligned} \boldsymbol{\omega}_m(f_a) = \Bigg[& \exp\left(j\frac{2\pi(f_a + f_{dc} + f)}{\lambda}{X'}_{u1}\right), \ldots, \\ & \exp\left(j\frac{2\pi(f_a + f_{dc} + f)}{\lambda}{X'}_{uv}\right), \ldots, \\ & \exp\left(j\frac{2\pi(f_a + f_{dc} + f)}{\lambda}{X'}_{uV}\right)\Bigg]^T_{V\times 1} \end{aligned} \quad (24)$$

where λ denotes the emission wavelength, T denotes the matrix transpose, f denotes the azimuth frequency center of different azimuth ambiguity components, and

$$f = \begin{cases} [-M/2 + m]f_{\text{PRF}}, M \in \{\text{even}\} \\ [-(M-1)/2 + m - 1]f_{\text{PRF}}, M \in \{\text{odd}\} \end{cases}.$$

The array vector matrix can be constructed as

$$\mathbf{A}(f_a) = [\boldsymbol{\omega}_1(f_a), \ldots, \boldsymbol{\omega}_M(f_a)]_{V\times M}. \quad (25)$$

The weight vector is

$$\mathbf{W}_m(f_a) = \mathbf{A}^+(f_a)\mathbf{e}_m \quad (26)$$

where $+$ denotes the pseudo inverse of the matrix and $e_m = [e_1, \cdots e_q, \ldots, e_M]^T$ $e_{q=m} = 1$, and $e_{q\neq m} = 0$.

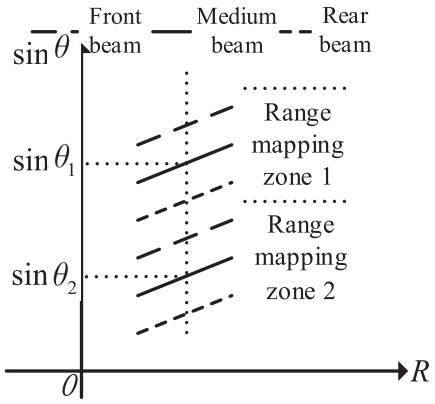

Fig. 8. Schematic diagram of range ambiguity.

Finally, for the *k*th segment subaperture signal received by the *u*th row array antenna, the matrix of echo signal of *V* azimuth channels goes to

$$\begin{aligned}\mathbf{S}_{u,k,\Delta}(t_r,f_a)=&[S_{u,k,1,\Delta}(t_r,f_a),\ldots,\\&S_{u,k,v,\Delta}(t_r,f_a),\ldots,\\&S_{u,k,V,\Delta}(t_r,f_a)]_{1\times V}\\&\Delta\in\{\text{spotlight},\text{stripe}\}.\end{aligned}\tag{27}$$

After multiplying (26) by (27), for the array antenna in the *u*th row and the *v*th column, the unambiguous signal in azimuth of the *k*th segment subaperture signal can be expressed as

$$\begin{aligned}S_{u,v,k,\Delta}(t_r,f_a)=&\sum_{n=1}^{N}w_{r,k,\Delta}(t_r)\times\\&W_{a,k,\Delta}(f_a+f_{dc})\times\\&\exp\left[-j2\pi(f_a+f_{dc})X_{n,\Delta}/v\right]\times\\&\exp\left[\frac{-j2\pi\times}{\frac{R_{k,B,n,\Delta}\sqrt{f_{aM}^2-(f_a+f_{dc})^2}}{v}}\right]\times\\&\exp(j2\pi f_a t_k)\times\exp(-j4\pi Y'_u\sin\theta_{n,\Delta}/\lambda)\\&\Delta\in\{\text{spotlight},\text{stripe}\}.\end{aligned}\tag{28}$$

C. Restoration of Unambiguity Signal in Range Based on Range DBF Technology

On the basis of Section IV-A and IV-B, large bandwidth signals without azimuth ambiguity are obtained by using azimuth bandwidth splicing. Meanwhile, only range ambiguity exists in the echo signals of each mode. The range ambiguity diagram is shown in Fig. 8. And there are two kinds of range ambiguity in the figure: one is caused when the instantaneous distance of scattering points in different pitching submapping bands meets certain conditions [38], and the other is caused when the instantaneous distance of scattering points from different azimuth sub mapping zones in the same pitching sub mapping zone meets certain conditions [39]. But when the azimuth ambiguity is removed from the signal, the latter range ambiguity does not exist. At this time, only the previous range ambiguity exists in the echo signal, which can be completely separated by the range DBF technology.

The ambiguity in range can be removed only when the freedom of range degree is not less than the number of range ambiguity. The process of removing ambiguity in range is as follows. For the *k*th segment subaperture signal, the array vector of *V* range channels can be written as

$$\begin{aligned}\boldsymbol{\chi}(\theta_n)=&\left[\exp\left(-j\frac{4\pi}{\lambda}Y'_1\sin\theta_n\right),\ldots,\right.\\&\exp\left(-j\frac{4\pi}{\lambda}Y'_u\ \sin\theta_n\right),\ldots,\\&\left.\exp\left(-j\frac{4\pi}{\lambda}Y'_U\ \sin\theta_n\right)\right]^T_{U\times 1},\\&\theta_n\in\{\theta_{n,\text{spotlight}},\theta_{n,\text{stripe}}\}\end{aligned}\tag{29}$$

where T is matrix transpose.

The array vector matrix can be constructed as

$$\begin{aligned}\boldsymbol{\zeta}(\theta_n)=&[\boldsymbol{\chi}(\theta_1),\ldots,\boldsymbol{\chi}(\theta_n),\ldots,\boldsymbol{\chi}(\theta_U)]_{U\times N},\\&\theta_n\in\{\theta_{n,\text{spotlight}},\theta_{n,\text{stripe}}\}.\end{aligned}\tag{30}$$

The weight vector is

$$\mathbf{v}(\theta_n)=\boldsymbol{\zeta}^{+}(\theta_n)\mathbf{e}_n,\ \theta_n\in\{\theta_{n,\text{spotlight}},\theta_{n,\text{stripe}}\}\tag{31}$$

where $+$ denotes the pseudo inverse of the matrix and $e_n=[e_1,\ldots,e_q,\cdots e_U]^T\ e_{q=n}=1,$ and $e_{q\neq n}=0$.

For the *k*th segment subaperture signal, the matrix of echo signal of *U* range channels can be expressed as

$$\begin{aligned}\mathbf{S}_{k,\Delta}(t_r,f_a)=&[S_{k,1,\Delta}(t_r,f_a),\ldots,\\&S_{k,u,\Delta}(t_r,f_a),\ldots,\\&S_{k,U,\Delta}(t_r,f_a)]_{1\times U},\\&\Delta\in\{\text{spotlight},\text{stripe}\}.\end{aligned}\tag{32}$$

After multiplying (31) by (32), the unambiguity signal of the *k*th subaperture in the *n*th pitching sub mapping zone can be obtained as

$$\begin{aligned}S_{n,k,\Delta}(t_r,f_a)=&w_{r,k,\Delta}(t_r)\times W_{a,k,\Delta}\left(f_a+f_{dc}\right)\\&\times\exp(j2\pi f_a t_k)\\&\times\exp\left[\frac{-j2\pi R_{k,B,n,\Delta}\sqrt{f_{aM}^2-\left(f_a+f_{dc}\right)^2}}{v}\right]\\&\times\exp(-j2\pi(f_a+f_{dc})X_{n,\Delta}/v)\\&\Delta\in\{\text{spotlight},\text{stripe}\}.\end{aligned}\tag{33}$$

In addition, the design conditions [14] of the antenna distance dimension D_r and the impact of actual ground fluctuation [39] on the range DBF performance should be noted.

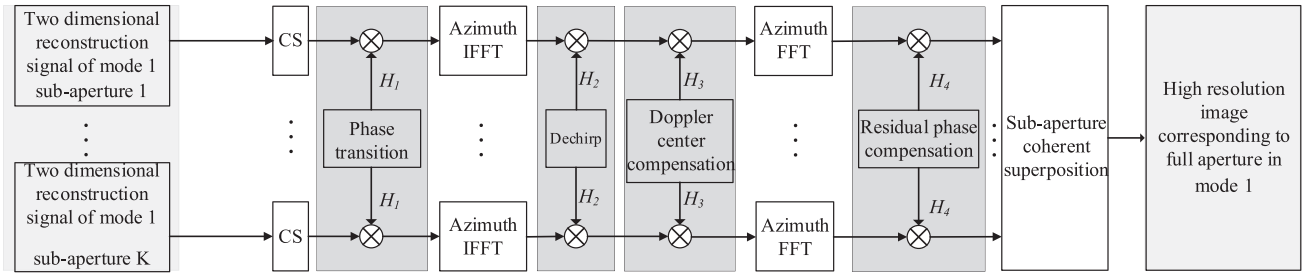

Fig. 9. Flow chart of subaperture fusion imaging (taking mode 1 as an example).

D. Coherent Fusion Imaging Algorithm Based on Subaperture Image

On the basis of Section IV-A–IV-C the article applies an imaging method [40] based on sub aperture complex image coherent fusion to spaceborne multimode MIMO-SAR. The coherent fusion imaging process of the subaperture image is shown in Fig. 9.

As shown in the Fig. 9, after the signal is reconstructed, the hyperbolic phase compensation function is defined as

$$H_{1,\Delta}(t_r, f_a) = \exp\left(j\frac{2\pi R_{k,B,n,\Delta}}{v}\sqrt{f_{aM}^2 - (f_a + f_{dc})^2}\right) \times \exp\left(-j\frac{\pi}{K_a}(f_a + f_{dc})^2\right) \quad \Delta \in \{\text{spotlight}, \text{stripe}\}. \tag{34}$$

After the reconstructed signal is compensated using the hyperbolic phase compensation function defined as (34), azimuth IFT is performed to the resulting expression and the signal becomes

$$S_{n,k,\Delta}(t_r, t_{\text{sub}} + t_k) = w_{r,k,\Delta}(t_r) \times a_{a,k,\Delta}(t_{\text{sub}} + t_k) \times \exp\left[j\pi K_a\left(t_{\text{sub}} + t_k - \frac{X_{n,\Delta}}{v}\right)^2\right] \times \exp\left[-j2\pi f_{dc}\left(t_{\text{sub}} + t_k\right)\right] \quad \Delta \in \{\text{spotlight}, \text{stripe}\}. \tag{35}$$

Transforming the hyperbolic phase of signal into the quadratic phase, the dechirp function can be expressed as

$$H_{2,\Delta}(t_r, t_{\text{sub}} + t_k) = \exp\left(-j\pi K_a(t_{\text{sub}} + t_k)^2\right) \quad \Delta \in \{\text{spotlight}, \text{stripe}\}. \tag{36}$$

It can be seen from (22) that the Doppler center of the subaperture signal of each mode has been compensated to zero. After the dechirp, the Doppler center of the subaperture signal of each mode is determined by H_2. Therefore, the Doppler center of the subaperture signals of each mode changes from $f_{dc} = 0$ to $f'_{dc} = -K_a t_k$.

After the quadratic phase of signal is compensated using the dechirp function defined as (36), the Doppler center recompensation function can be written as

$$H_{3,\Delta}\left(t_r, t_{\text{sub}} + t_k\right) = \exp\left(-j2\pi f'_{dc}\left(t_{\text{sub}} + t_k\right)\right) \quad \Delta \in \{\text{spotlight}, \text{stripe}\}. \tag{37}$$

After the Doppler center of subaperture signal is recompensated using the Doppler center recompensation function defined as (37), azimuth FT is performed to the resulting expression and the signal can be obtained as

$$S_{n,k,\Delta}(t_r, f_a) = w_{r,k,\Delta}(t_r) \times \exp\left(-j2\pi K_a \frac{X_{n,\Delta}}{v} t_k\right) \times W_{a,k,\Delta}(f_a + f_{dc}) \times \exp\left[j\pi K_a\left(\frac{X_{n,\Delta}}{v}\right)^2\right] \quad \Delta \in \{\text{spotlight}, \text{stripe}\}. \tag{38}$$

It can be seen from (38) that the phase of the subaperture focusing signal of each mode is a linear phase with respect to t_k. However, the linear phase of (38) is not a constant at the focusing frequency point $f_a = \frac{-K_a X_{n,\Delta}}{v}$ $\Delta \in \{\text{spotlight}, \text{stripe}\}$, which leads to the different phases of the focusing signals of different subapertures at the focusing frequency point, and finally makes the subaperture images unable to be coherently accumulated. Therefore, the phase compensation function can be constructed as

$$H_{4,\Delta}(t_r, f_a) = \exp(-j2\pi f_a t_k), \Delta \in \{\text{spotlight}, \text{stripe}\}. \tag{39}$$

After the signal is compensated using the phase compensation function defined as (39), the subaperture image can be written as

$$S_{n,k,\Delta}(t_r, f_a) = w_{r,k,\Delta}(t_r) \times \exp\left[-j2\pi\left(f_a + K_a\frac{X_{n,\Delta}}{v}\right)t_k\right] \times W_{a,k,\Delta}(f_a + f_{dc}) \times \exp\left[j\pi K_a\left(\frac{X_{n,\Delta}}{v}\right)^2\right] \quad \Delta \in \{\text{spotlight}, \text{stripe}\}. \tag{40}$$

On the basis of $f_a + \frac{K_a X_{n,\Delta}}{v} = 0, \Delta \in \{\text{spotlight}, \text{stripe}\}$, the phase of focusing signal of subaperture is identical at the focus frequency, and also is linear with respect to t_k at nonfocusing frequencies. Thus, it is possible to coherently fuse all low-resolution complex images into high-resolution complex images.

TABLE I
ORBITAL PARAMETERS

Parameter	Value
Orbital altitude	531 km
Semimajor axis	7295 km
Right ascension of ascending node	219.54°
Inclination	96.74°
Argument of perigee	78.5°
Eccentricity	0.0014

TABLE II
SIMULATION PARAMETERS OF MULTIMODE SYSTEM MODEL

Parameter	Value
Mode	2
Bandwidth of spotlight mode	200 MHz
Bandwidth of strip mode	50 MHz
Carrier frequency	9.65 GHz
Number of subapertures signals	8
Sub pulse duration	20 us
Width of surveying and mapping zone	120 km
The height of radar	700 km
Available velocity	7000 m/s
Incident angle	30°
Pulse repetition frequency	1680 Hz
Range sampling rate	360 MHz

V. EXPERIMENT RESULTS

In this section, simulation experiments are used to verify the imaging performance, multiresolution characteristics, and the effectiveness of the improved APC of the imaging mode in this article. Assuming that the total height of the array antenna is 0.40 m and the total azimuth length is 24 m. The large array antenna is evenly divided into 2×3 subapertures. In addition, the pulses duration is equally divided into six sub pulses. The orbital parameters are listed in Table I and the simulation parameters of radar system are given in Table II. The "8" in Table II represents the number of subaperture signals into which the full-aperture signal is divided.

A. Multimode Echo Separation Experiment With Improved APC

In order to better demonstrate the effectiveness of the improved APC, the multimode echo separation simulation experiment is carried out for full aperture single targets. Assuming that the single target of each pitching submapping zone is located in the center of scene of each pitching submapping zone, the two modes simultaneously image them, as shown in Fig. 10. Fig. 10(a) shows the results after azimuth phase demodulation of the echo signal in one of the receiving channels. It can be seen that the azimuth spectrum of the two modes is aliased, and the Doppler frequency shift of azimuth spectrum of the stripe mode is $F_{\mathrm{PRF}}/2$ after phase demodulation. Then after azimuth DBF processing, the echo signals of the two modes are completely separated, as shown in Fig. 10(b) and (c).

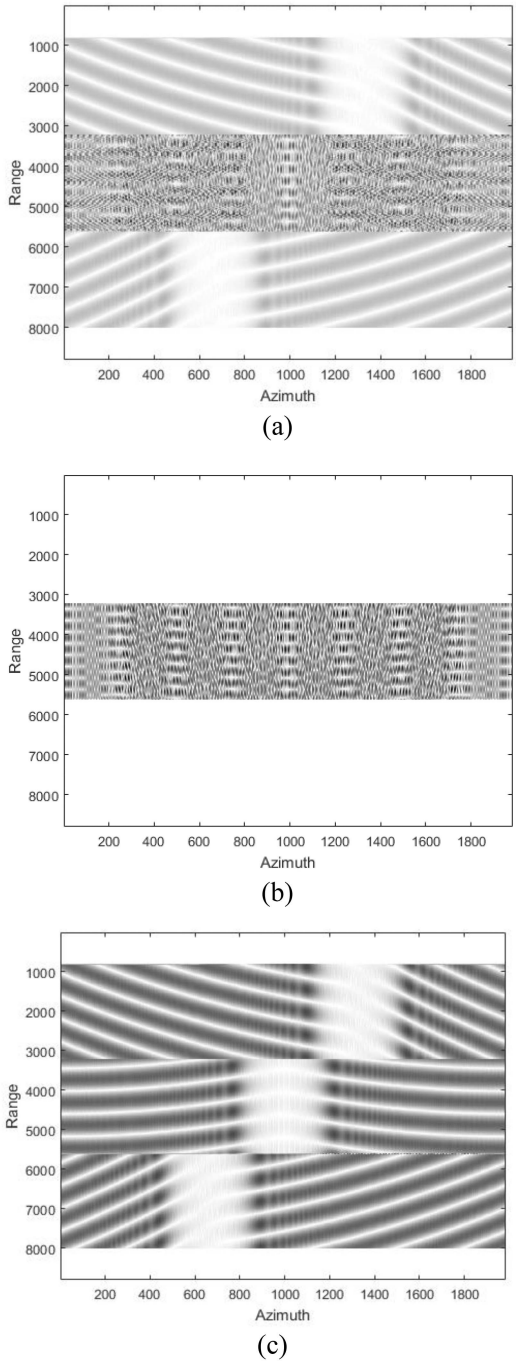

Fig. 10. Separation experiment of multimode echo Doppler. (a) Echo Doppler before separation. (b) Echo Doppler of spotlight mode after separation. (c) Echo Doppler of stripe mode after separation.

B. Analysis of Echo Separation Time

After demonstrating the effectiveness of the improved APC, a comparative experiment is conducted between the improved and original APC methods in separating multimode echoes. Table III presents the processing time of utilizing both methods in separating multimode echoes. It can be obtained from the table that the improved APC method spends less time to separate multimode echoes than the original APC method, verifying that the superiority of the improved APC method.

TABLE III
PROCESSING TIME OF ECHO SEPARATION OF MULTIMODE

Method	The processing time of echo separation of multimode
APC	423.653456 s
Improved APC	339.683324 s

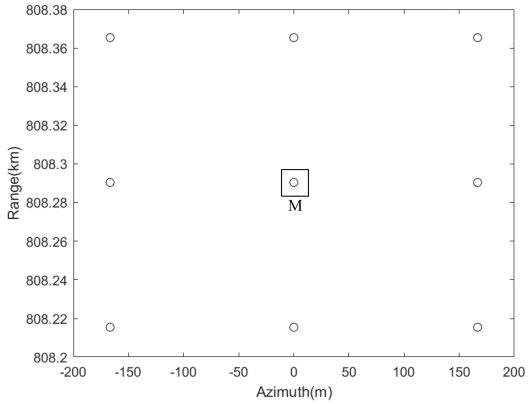

Fig. 11. Lattice distribution of the point targets.

TABLE IV
PSLR AND ISLR OF EACH MODE POINT TARGET

Mode	Point target	Range	
		PSLR (dB)	ISLR (dB)
Stripe	M (Original APC)	-13.29	-9.55
	M (Improved APC)	-13.36	-9.58
Spotlight	M (Original APC)	-13.35	-9.61
	M (Improved APC)	-13.36	-9.63

TABLE V
PSLR AND ISLR OF EACH MODE POINT TARGET

Mode	Point target	Azimuth	
		PSLR (dB)	ISLR (dB)
Stripe	M (Original APC)	-13.87	-9.76
	M (Improved APC)	-12.93	-9.80
Spotlight	M (Original APC)	-13.22	-10.05
	M (Improved APC)	-13.24	-10.06

C. Imaging Quality With Original and Improved APC

After verifying that the improved APC method can spend less time to separate multimode echoes than the original APC method, a comparative experiment is conducted between the improved and original APC methods in imaging results. Fig. 11 shows the 3×3 distributed lattice in the first pitching mapping belt. Fig. 12 shows the imaging results of point target by using original and improved APC methods. Table IV shows the integral side-lobe ratio and peak side-lobe ratio in range before and after imaging the point target for both methods. Table V shows the integral side-lobe ratio and peak side-lobe ratio in azimuth before

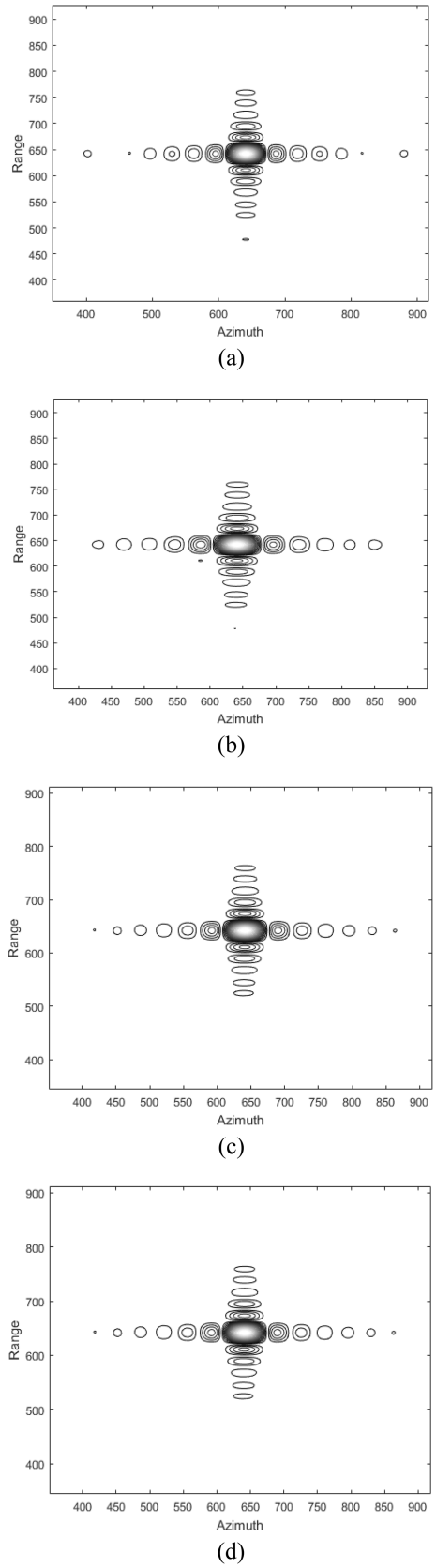

Fig. 12. Contour map of point target M (a) of stripe mode after using original APC, (b) of stripe mode after using improved APC, (c) of spotlight mode after using original APC, and (d) of spotlight mode after using improved APC.

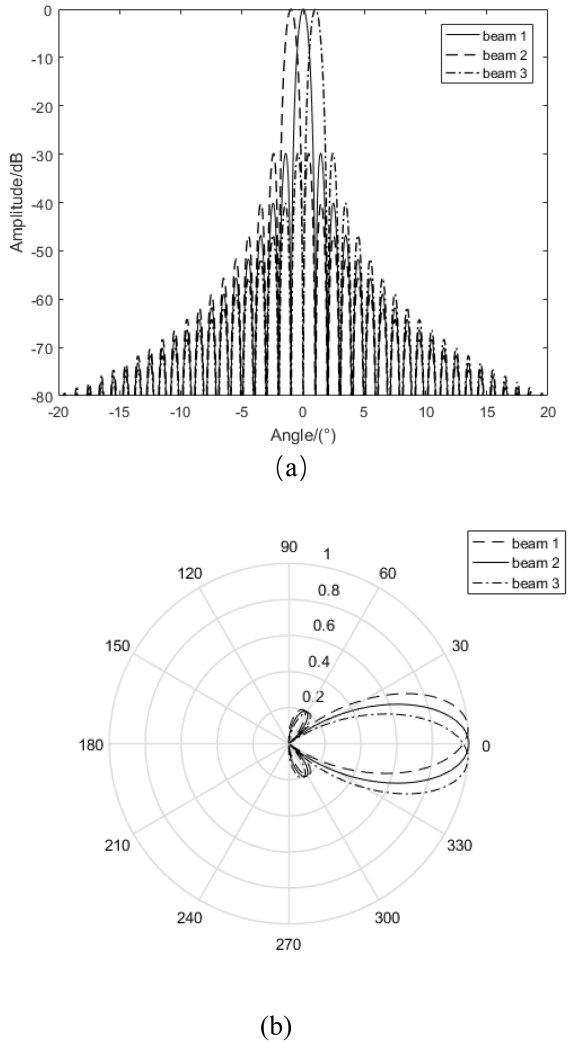

Fig. 13. Antenna pattern for the first three subbeams. (a) System of rectangular coordinates. (b) System of polar coordinates.

and after imaging the point target for both methods. Simulation results show that the improved APC does not affect the quality of SAR imaging.

D. Effectiveness of Removing Ambiguity

On the basis of Section IV-A, in order to better evaluate the effect of removing ambiguity in azimuth and range, the experiment is only carried out for stripe mode with single targets of full aperture. Fig. 13 records the data of subbeam 1–3 received by the antenna. According to the antenna pattern, the main lobe of the antenna pattern is clear and the side lobes are all −30 dB, indicating no inherent error. It can be seen that the antenna pattern has no effect on removing ambiguity in this article. After compensating the Doppler frequency shift, Fig. 14 shows the Doppler spectra of echoes before and after removing ambiguity in azimuth. The subbeam signals in azimuth are separated by using the spatial filtering that is proposed in this article, as shown in Fig. 14(b)–(d).

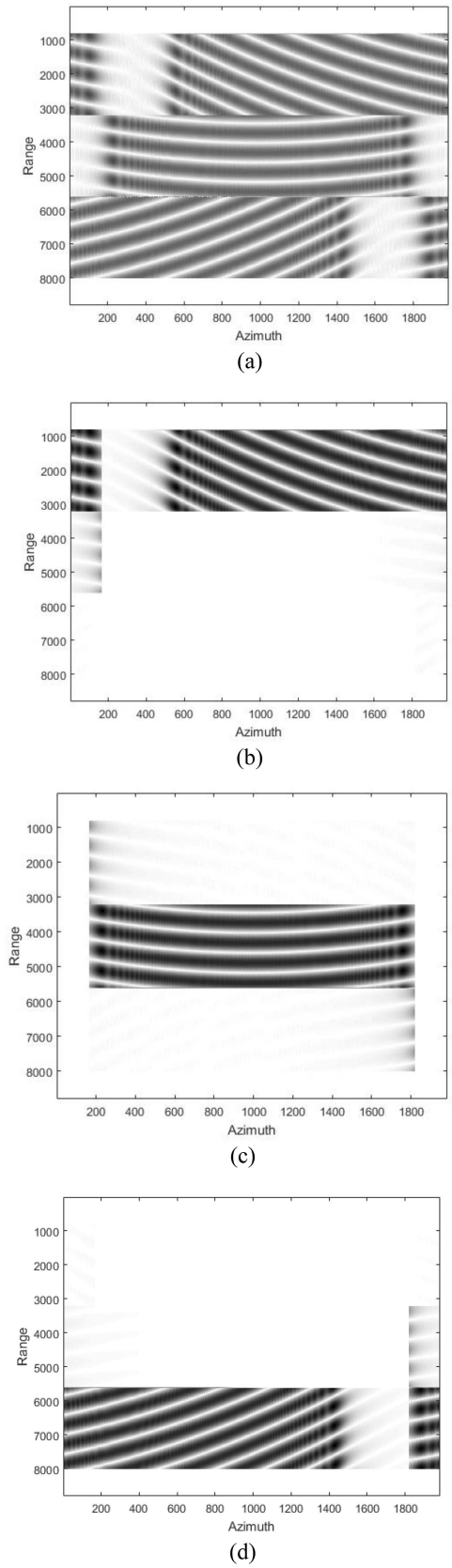

Fig. 14. Doppler spectra of echoes before and after removing ambiguity in azimuth. (a) Doppler spectra after compensating the Doppler frequency shift. (b) Front beam after removing ambiguity in azimuth. (c) Medium beam after removing ambiguity in azimuth. (d) Rear beam after removing ambiguity in azimuth.

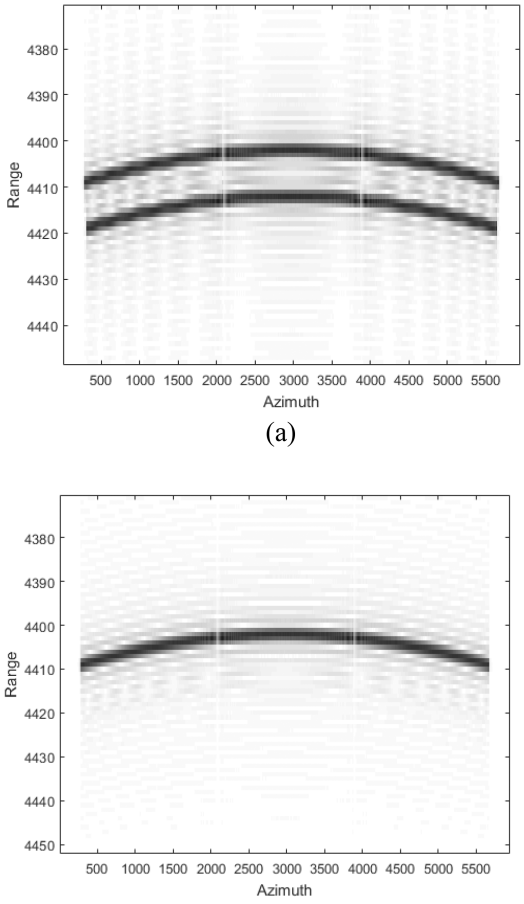

Fig. 15. Range compression result of echoes before and after removing ambiguity in range. (a) Result before removing ambiguity in range. (b) Result after removing ambiguity in range.

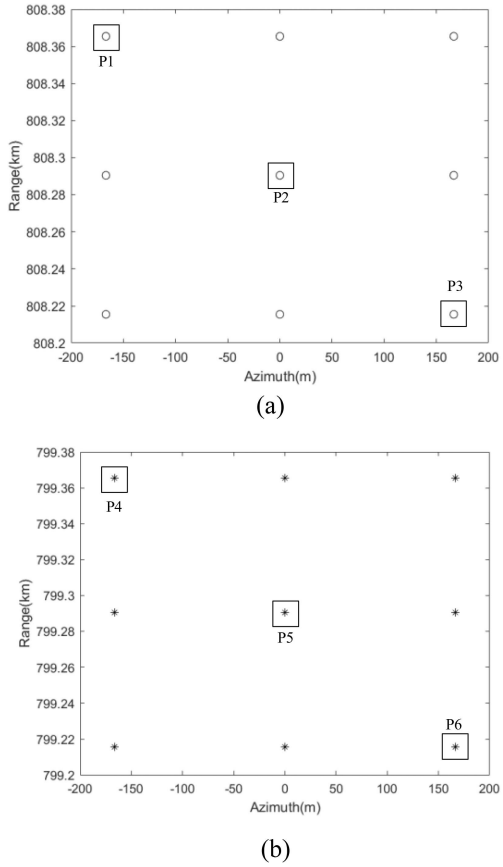

Fig. 16. Lattice distribution of the point targets. (a) First pitching mapping belt. (b) Second pitching mapping belt.

After compensating the transmitting delay of different azimuth subbeams, the large bandwidth signals without ambiguity in azimuth are obtained by using bandwidth splicing. Fig. 15 shows the range compression result of echoes before and after removing ambiguity in range. The signals in range are separated by using the range DBF technology that is proposed in this article, as shown in Fig. 15(b).

E. Latticed Target Imaging Experiment

After verifying the effectiveness of the improved APC method, the imaging simulation of the latticed target is carried out. Fig. 16 shows the distribution of the latticed target. Fig. 16(a) shows the 3×3 distributed lattice in the first pitching mapping belt. The azimuth spacing of each target point is 166.67 m, and the range spacing point of each target is 151.70 m. At the same time, the coordinates of the three marked points are $P_1(-166.67\,\mathrm{m}, R_{s1} + 151.70\,\mathrm{m}), P_2(0\,\mathrm{m},\ R_{s1}\,\mathrm{m})$ and $P_3(166.67\,\mathrm{m}, R_{s1} - 151.70\,\mathrm{m})$ respectively. Fig. 16(b) shows the 3×3 distributed lattice in the second pitching mapping belt. The azimuth spacing of each target point is 166.67 m, and the range spacing of each target is 151.70 m. Meanwhile, the coordinates of the three marked points are $P_4(-166.67\,\mathrm{m}, R_{s2} + 151.70\,\mathrm{m}), P_5(0\,\mathrm{m}, R_{s2}\,\mathrm{m}), P_6(166.67\,\mathrm{m}, R_{s2} - 151.70\,\mathrm{m})$ respectively. Where R_{s1} is the shortest slant distance of the scene center of the first pitching mapping belt and R_{s2} denotes the shortest slant distance of the scene center of the second pitching mapping belt.

In this article, the imaging simulation experiment is only carried out for the lattice in the first pitching mapping belt of each mode. The simulation results on the latticed target are shown in Figs. 17 –19. Fig. 17(a) and (b) show the azimuth profile of a point target after imaging fusion in stripe mode and spotlight mode, respectively. It can be seen from the figures that the azimuth resolution of the fused image gradually increases with the increase of the number of subaperture images, which shows the effectiveness of the subaperture image fusion algorithm in this system configuration.

Figs. 18 and 19 show the contour map of the final image of the three targets (P_1, P_2, and P_3) in stripe mode and spotlight mode, respectively. Table VI analyzes the integral side-lobe ratio (ISLR), peak side-lobe ratio (PSLR) and resolution (approximate value after multiple measurements at a single point) of the imaging results of the three targets in each mode. The imaging effect of the two modes is good for both point (P_2) in scene center and point (P_1 and P_3) in scene edge. Therefore, the result shows that the subaperture fusion algorithm has good imaging performance in this imaging mode.

TABLE VI
PSLR AND ISLR OF EACH MODE POINT TARGET

Mode	Point target	Range		Azimuth		Resolution	
		PSLR (dB)	ISLR (dB)	PSLR (dB)	ISLR (dB)	Azimuth(m)	Range(m)
Stripe mode	P_1	-13.37	-9.59	-12.95	-9.81	4	3
	P_2	-13.36	-9.58	-12.93	-9.80	4	3
	P_3	-13.33	-9.54	-12.92	-9.79	4	3
Spotlight mode	P_1	-13.37	-9.59	-13.25	-9.98	2	0.75
	P_2	-13.36	-9.63	-13.24	-10.06	2	0.75
	P_3	-13.40	-9.55	-13.27	-9.99	2	0.75

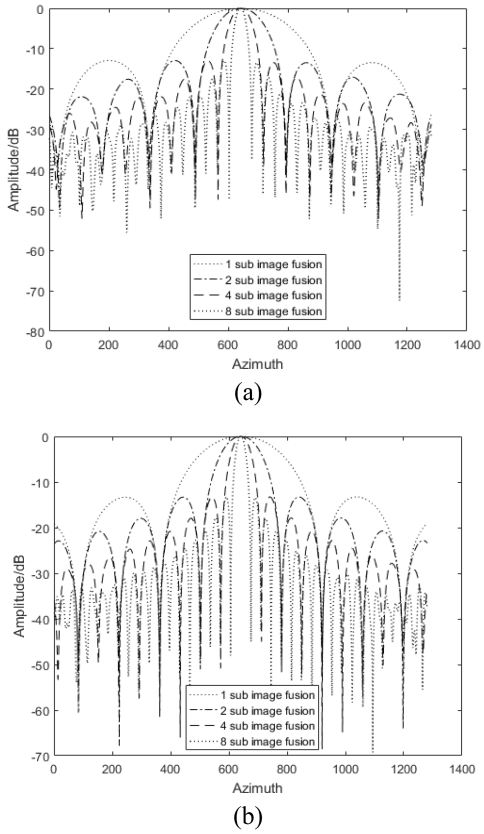

Fig. 17. Azimuth profile of point target after imaging fusion (a) of stripe mode and (b) of spotlight mode.

TABLE VII
SIMULATION PARAMETERS OF MULTIMODE SYSTEM MODEL

Parameter	Value
Carrier frequency	9.65 GHz
Sub pulse duration	20 us
Width of surveying and mapping zone	120 km
The height of radar	700 km
Available velocity	7000 m/s
Incident angle	30°
Pulse repetition frequency	1680 Hz
Range sampling rate	360 MHz

TABLE VIII
SIMULATION PARAMETERS OF BANDWIDTH OF EACH MODE

Model	Bandwidth	Value
Literature [18],[19], [20]	TOPS	50 MHz
	Sliding spotlight	200 MHz
Literature [21]	TOPS	50 MHz
	Spotlight	200 MHz
Ours	Stripe	50 MHz
	Spotlight	200 MHz

F. Imaging Performance Analysis

In the experiments, the echo SNR and maximum pitching mapping belt of the imaging mode proposed in this article and the imaging mode proposed in [18], [19], [20], and [21] are compared and analyzed. The SNR of the system is proportional to the transmitting area and the receiving area. In addition, the maximum pitching mapping belt of the system is related to the range swath width of the transmitted signal model scanning. The simulation parameters of the radar system are given in Table VII. The parameters of bandwidth of each mode are given in Table VIII.

Fig. 20 shows the distribution of latticed target. Fig. 20(a) shows the 3×3 distributed lattice in the first pitching mapping belt. Fig. 20(b) shows the 3×3 distributed lattice in the second pitching mapping belt. The simulation results on the point target are shown in Fig. 21. Fig. 21(a) and (b) show the imaging result of point target of [18], [19], and [20]. Fig. 21(c) and (d) show the imaging result of point target of [21]. Fig. 21(e)–(h) show the imaging result of point target in this article. It can be seen that the imaging results of [18], [19], [20], [21], and in this article are good.

Table IX analyzes the ISLR, PSLR, and SNR of the imaging results of the point target in each mode. The imaging effect of each mode is good for point (Q_1 and Q_2). In addition, the multimode imaging model in this article has a larger pitching mapping belt than the multimode imaging model in [18], [19], [20], and [21]. Therefore, it can be concluded that the multimodal imaging model in this article has a higher SNR and a wider pitching mapping belt.

G. Multiresolution Imaging Performance Analysis

After verifying the imaging performance of the latticed target, the multiresolution characteristic of the imaging configuration is simulated in the latticed scene. According to the Table II, the range resolution of the stripe mode is 3 m, and the azimuth

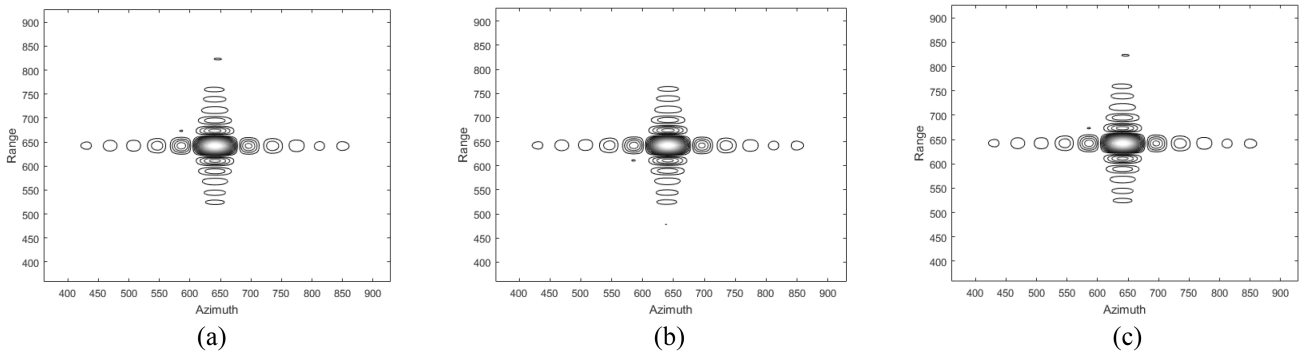

Fig. 18. Point target imaging results after subaperture fusion in stripe mode. (a) Contour map of point target P_1. (b) Contour map of point target P_2. (c) Contour map of point target P_3.

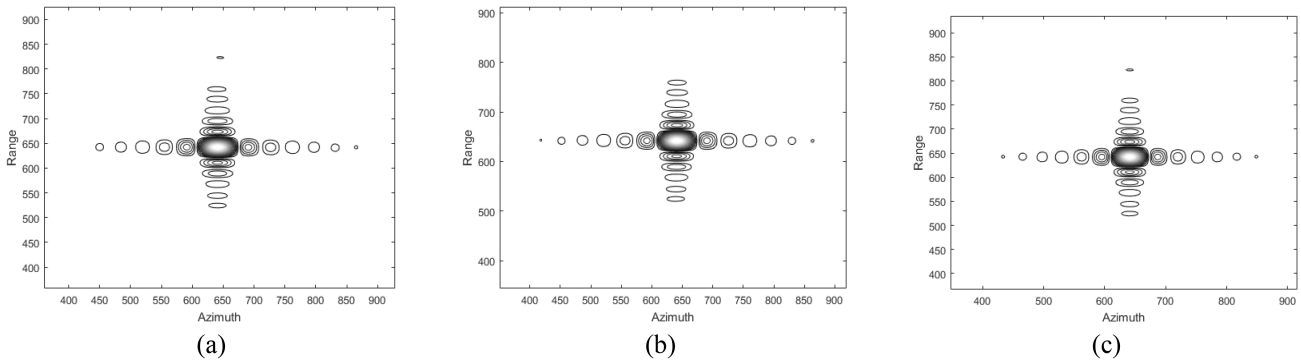

Fig. 19. Point target imaging results after subaperture fusion in spotlight mode. (a) Contour map of point target P_1. (b) Contour map of point target P_2. (c) Contour map of point target P_3.

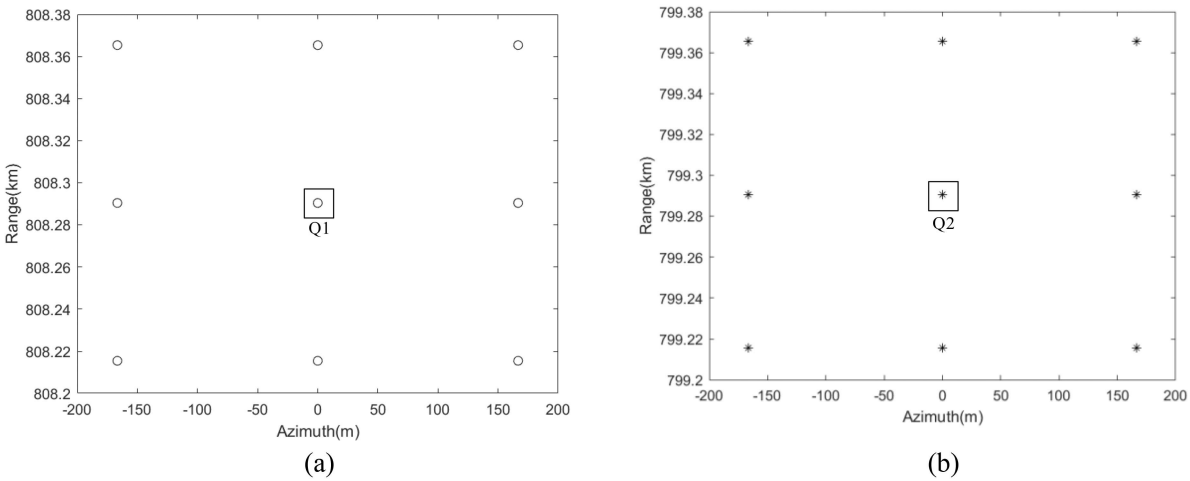

Fig. 20. Lattice distribution of the point targets. (a) First pitching mapping belt. (b) Second pitching mapping belt.

resolution of the stripe mode is 4 m. The range resolution of the spotlight mode is 0.75 m, and the azimuth resolution of the spotlight mode is 2 m. From Fig. 16(a), the point target of P_2 is redesigned. The point of P_2 has been changed from a single target to a 3×3 uniformly distributed lattice, with the azimuth and range spacing of 2.5 m, as shown in Fig. 22. Limited to the length of the article, the imaging simulation experiment is only conducted for the latticed scene of the first pitching mapping zone.

Fig. 23 presents the imaging results of the dotted scene in Fig. 22. Fig. 23(a) shows the imaging results of imaging fusion of the P_2 lattice in the stripe mode, and Fig. 23(b) shows the imaging results of imaging fusion of the P_2 lattice in the spotlight mode. It can be seen in Fig. 23 that the spotlight mode can clearly separate the nine targets of P_2 lattice, while the stripe mode fails to effectively distinguish targets due to the resolution.

In order to better show the multiresolution imaging performance, this article takes any 3×1 distributed lattice

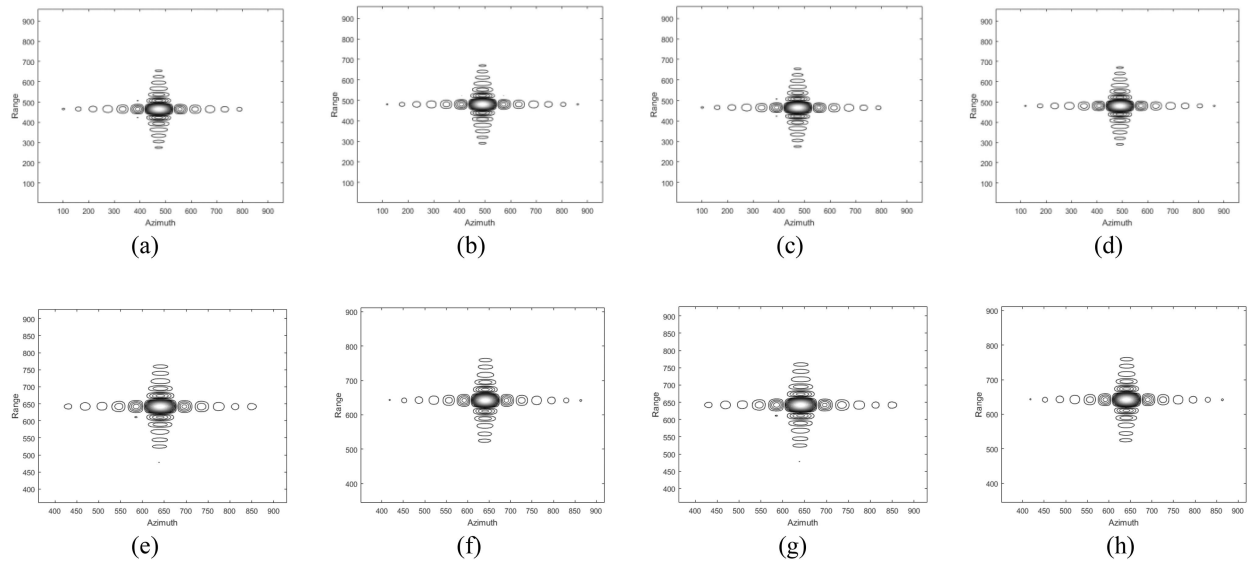

Fig. 21. Imaging results of point target. (a) Contour map of point target Q_1 of TOPS mode in [18], [19], and [20]. (b) Contour map of point target Q_1 of sliding spotlight mode in [18], [19], and [20]. (c) Contour map of point target Q_1 of TOPS mode in [21]. (d) Contour map of point target Q_1 of spotlight mode in [21]. (e) Contour map of point target Q_1 of stripe mode in this article. (f) Contour map of point target Q_1 of spotlight mode in this article. (g) Contour map of point target Q_2 of spotlight mode in this article. (h) Contour map of point target Q_2 of spotlight mode in this article.

TABLE IX
PSLR AND ISLR OF EACH MODE POINT TARGET

Model	Mode	Point target	Range		Azimuth		SNR(dB)
			PSLR (dB)	ISLR (dB)	PSLR (dB)	ISLR (dB)	
Literature [18] ,[19], [20]	TOPS	Q_1	-13.17	-9.52	-12.99	-9.86	**-5.35**
	Sliding spotlight	Q_1	-13.19	-9.57	-12.93	-9.94	**-5.78**
Literature [21]	TOPS	Q_1	-13.16	-9.53	-12.98	-9.91	**-5.32**
	Spotlight	Q_1	-13.27	-9.58	-13.17	-9.99	**-6.07**
Ours	Stripe	Q_1	-13.36	-9.58	-12.93	-9.80	**-15.78**
		Q_2	-13.37	-9.60	-12.94	-9.83	**-15.88**
	Spotlight	Q_1	-13.36	-9. 63	-13.24	-10.06	**-16.54**
		Q_2	-13.40	-9.70	-13.32	-9.99	**-16.47**

The bold entities are to illustrate that the imaging mode in this paper has a higher SNR than the imaging mode in literature [18-21].

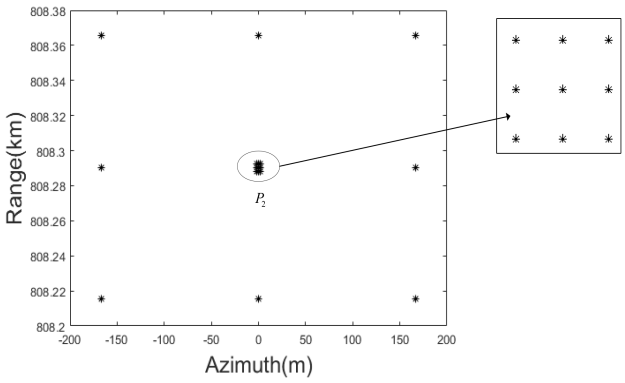

Fig. 22. Target distribution in latticed scene.

in Fig. 22 as a new imaging scene and performs range sampling on the imaging results. Fig. 24(a) is the result of the range sampling in stripe mode, and Fig. 24(b) is the result of the range sampling in spotlight mode. It can be seen from Fig. 24 that the spotlight mode can intuitively separate three targets, while the stripe mode is unable to effectively distinguish targets due to resolution constraints. Therefore, Figs. 16–24 show that the multiresolution characteristics and imaging effect of the proposed model are good.

H. Surface Targets Simulation

Due to the lack of spaceborne multimodal SAR data with high-resolution and wide-swath, the surface simulation is adopted to further verify the multiresolution performance of the proposed model. In the high-frequency approximation, it can be known that the backscattering coefficient of each target can be assumed to be constant when the frequency and scattering of each target is all-directional [34]. Thus, relying on reflection coefficients of the real SAR image to obtain credible echo data is the most critical step. This article uses the gray values of the real SAR

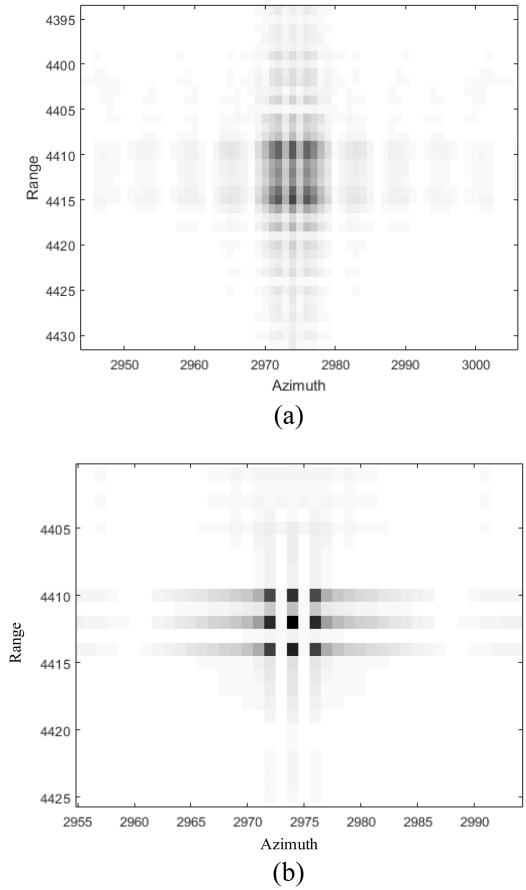

Fig. 23. Imaging results of the P_2 lattice (a) in stripe mode and (b) in spotlight mode.

TABLE X
PSLR AND ISLR OF THE RED BOX AREAS

Figure	The red box areas	PSLR (dB)	ISLR (dB)
Fig.26(a)	C	-12.42	-9.50
	D	-12.46	-9.48
Fig. 26(b)	C	-13.60	-10.02
	D	-13.64	-10.07

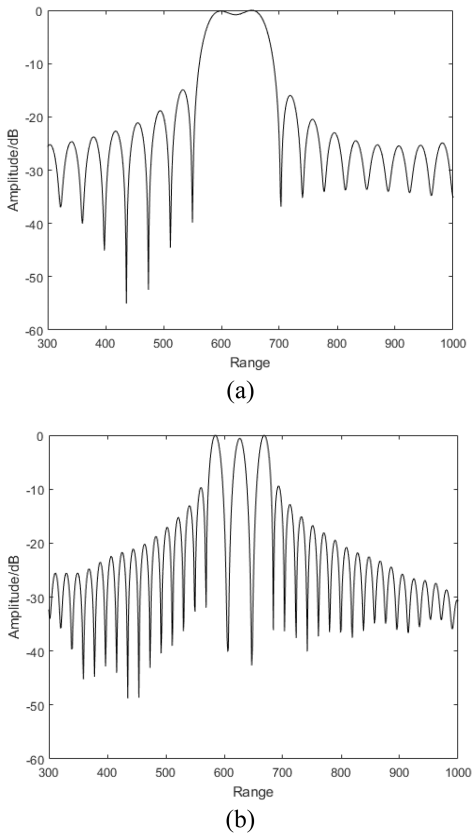

Fig. 24. Range sampling after image fusion (a) in stripe mode and (b) in spotlight mode.

TABLE XI
RESOLUTION OF THE RED BOX AREAS

Figure	The red box areas	Azimuth (m)	Range (m)
Fig.26(a)	B	4	3
	C	4	3
	D	4	3
Fig. 26(b)	B	2	0.75
	C	2	0.75
	D	2	0.75

image to represent the amplitude of the backscatter coefficient. In addition, radar system parameters in ground target simulation are the same as those in target simulation. And after the echo of surface targets is obtained, it can be processed through the signal processing flow, which is proposed in this article. The imaging results are shown in Fig. 25(b) and (c)

To further verify the multiresolution performance of the proposed model. A local image containing nine highlight points is set in the original SAR image, that is, the red box area marked A in Fig. 25(b) and (c). Fig. 26(a) and (b) are enlarged images of the red box area marked A in Fig. 25(a) and (b), respectively. Table X analyzes the ISLR and PSLR of the imaging results of the red box areas marked C and D in Fig. 26(a) and (b). It can be seen from Table X that the PSLR and ISLR of red box areas marked C and D in Fig. 26(b) are higher than those of red box areas marked C and D in Fig. 26(a), indicating that the imaging quality of the spotlight mode is much better than that of the stripe mode. In addition, Table XI presents the resolution in azimuth and range of red box areas marked B, C, and D in Fig. 26(a) and (b). From the comparison between the red box area marked B in Fig. 26(a) and (b), nine highlighted point targets can be clearly distinguished in the spotlight mode, while they cannot be effectively distinguished due to the limited resolution in the stripe mode. Therefore, the reliability and availability of the proposed multiresolution imaging model can be verified.

VI. DISCUSSION

The premise of the aforementioned simulation results assumes an ideal state for each channel, without considering the differences and interferences between channels in actual work. On the one hand, it is inevitable for channel errors to exist in practical radar systems [41]. Due to the factors,

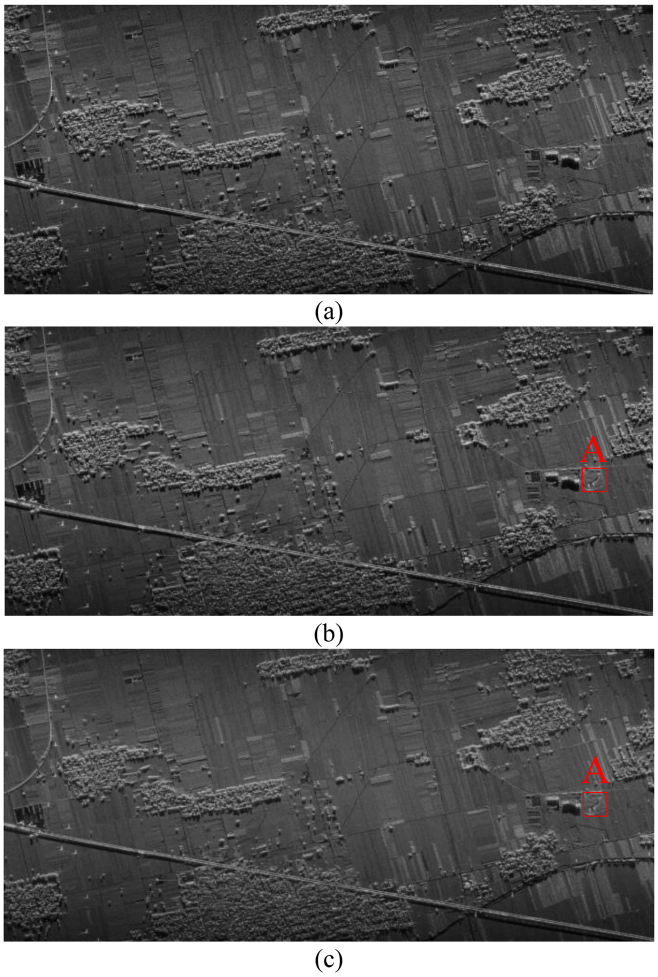

(a) (b) (c)

Fig. 25. Simulation results of the surface targets. (a) Reference terrain scene. (b) Imaging result of stripe model. (c) Imaging result of spotlight model.

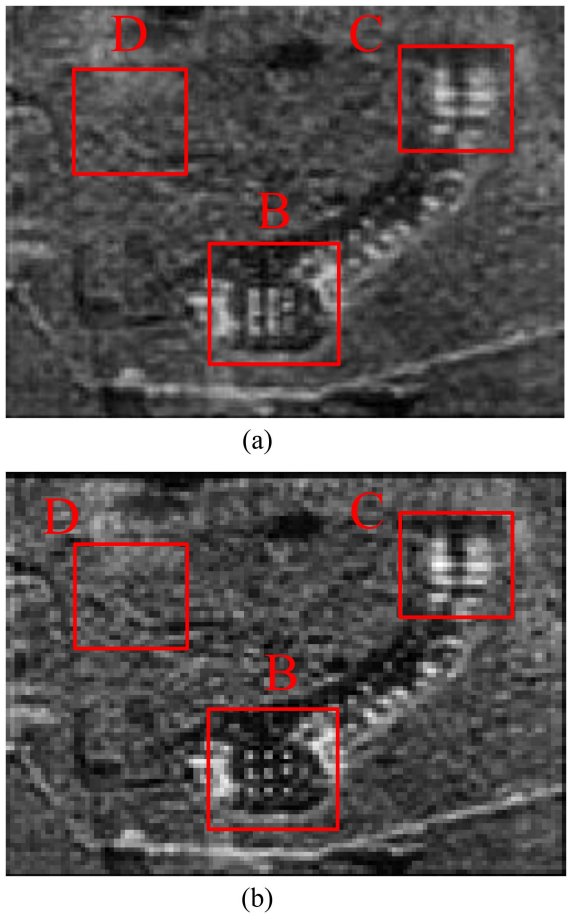

(a) (b)

Fig. 26. Enlarged images of the area marked area in Fig. 25. (a) Enlarged image of the marked area in Fig. 25(b). (b) Enlarged image of the marked area in Fig. 25(c).

such as temperature, power supply voltage, and manufacturing processes, the frequency response functions transmitted by each channel cannot maintain good consistency, that is, channel mismatch. It will reduce the performance of the system and have errors after imaging processing. However, these issues can be resolved by the method of the channel equalization. Thus, a channel equalizer is required on the hardware configuration of the radar system. On the other hand, with the increasing complexity of radar system functions, the number of receiving and transmitting antennas on the same platform is increasing. Receiving and transmitting with multiple antennas inevitably results in mutual interference, which reduces antenna isolation and communication capacity [42]. Thus, a device of channel isolation is required in the hardware configuration of the radar system to avoid interference between each channel.

In the actual working conditions, in order to maximize the gain of the range DBF in the useful signal direction and make the zero point to the adjacent subpulse echo direction, it is necessary that the narrow beamwidth formed by the range DBF is smaller than the angle of the echo direction between the adjacent subpulses. Therefore, the actual antenna size in range needs to meet the condition [39]

$$D_r \geq 2\lambda R_{\text{far}} \tan\theta_{\max}/(c\Delta T_{\min}) \tag{41}$$

where R_{far} denotes the slant distance at the farthest end of the scene, $\theta_{\max}$ represents the maximum angle of squint, and $\Delta T_{\min}$ represents the delay of minimum time between echoes of different pitching mapping belts that belong to the same azimuth subbeam signal.

VII. Conclusion

This article proposes a simultaneous multiresolution imaging mode based on multimode MIMO-SAR. First, an improved APC technology is used to separate multimode echo signals. Then spatial filtering technology and range digital beamforming technology are used to remove the azimuth ambiguity and range ambiguity of the subaperture signals. Finally, the high-resolution images corresponding to the full aperture of each mode are obtained through the subaperture image coherent fusion algorithm. The improved APC reduces the computation and complexity on the basic of effectively separating multimode echo signals. The combination of subaperture division technology and subaperture image coherent fusion algorithm greatly reduces the amount of data in the imaging system. The proposed imaging mode not only satisfies the requirements of high-resolution wide-swath imaging, but also obtains different resolution imaging areas in one imaging processing. This optimizes the utilization of the antenna transmission area and enhances the utilization of

transmission channels. Simulation results show that the improved APC can effectively separate multimode echo signals, and the multiresolution characteristics and imaging effect of the proposed model are good, which verifies the feasibility and effectiveness of the system configuration.

REFERENCES

[1] A. Freeman et al., "The 'Myth' of the minimum SAR antenna area constraint," *IEEE Trans. Geosci. Remote Sens.*, vol. 38, no. 1, pp. 320–324, Jan. 2000.

[2] W. Q. Wang, "Large-area remote sensing in high-altitude high-speed platform using MIMO SAR," *IEEE J. Sel. Topics Appl. Earth Observ. Remote Sens.*, vol. 6, no. 5, pp. 2146–2158, Oct. 2013.

[3] L. Wang, P. Huang, X. Liu, R. Wang, Y. Liu, and H. Xu, "A novel multichannel high-resolution imaging method for MIMO-SAR system based on filterbank framework reconstruction theory," in *Proc. 6th Asia-Pacific Conf. Synthetic Aperture Radar*, 2019, pp. 1–6.

[4] L. Kang, L. Sun, Q. Zhang, T.-Y. Li, F.-F. Gu, and B.-S. Liang, "A novel 3D imaging method for downward-looking MIMO-SAR based on LQ regularization," in *Proc. CIE Int. Conf. Radar*, 2016, pp. 1–4.

[5] Z. Rahimi, F. Othman, and A. R. M. Shariff, "Improving geometric construction of high-resolution SAR images using Kriging-based surrogate modelling in mountainous terrain of Malaysia," *Int. J. Remote Sens.*, vol. 42, no. 22, pp. 8624–8639, 2021.

[6] M. AlShaya, M. Yaghoobi, and B. Mulgrew, "Ultrahigh resolution wide swath MIMO-SAR," *IEEE J. Sel. Topics Appl. Earth Observ. Remote Sens.*, vol. 13, pp. 5358–5368, 2020.

[7] W. Xu, Y. K. Deng, and R. Wang, "Multichannel synthetic aperture radar systems with a planar antenna for future spaceborne microwave remote sensing," *IEEE Aerosp. Electron. Syst. Mag.*, vol. 27, no. 12, pp. 26–30, Dec. 2012.

[8] Y. J. Zhao, X. Y. Lu, M. Ritchie, W. M. Su, and H. Gu, "Suppression of sidelobes in MIMO radar with distinctive piecewise non-linear frequency modulation sub-carrier," *Int. J. Remote Sens.*, vol. 41, no. 1, pp. 353–372, 2020.

[9] G. D. Callaghan and I. D. Longstaff, "Wide-swath space-borne SAR and range ambiguity," in *Proc. Radar*, 1997, pp. 248–252.

[10] G. C. Sun, M.-D. Xing, X.-G. Xia, Y.-F. Wu, and Z. Bao, "Multichannel full-aperture azimuth processing for beam steering SAR," *IEEE Trans. Geosci. Remote Sens.*, vol. 51, no. 9, pp. 4761–4778, Sep. 2013.

[11] M. Suess, B. Grafmueller, and R. Zahn, "A novel high resolution, wide swath SAR system," in *Proc. Scanning Present Resolving Future. Proc. IEEE Int. Geosci. Remote Sens. Symp.*, 2001, pp. 1013–1015.

[12] F. Bordoni, M. Younis, and G. Krieger, "Ambiguity suppression by azimuth phase coding in multichannel SAR systems," *IEEE Trans. Geosci. Remote Sens.*, vol. 50, no. 2, pp. 617–629, Feb. 2012.

[13] Q. Wu, M. Xing, B. Liu, and Z. Bao, "Swath imaging with the plane-array MIMO-SAR system," *Acta Electronica Sinica*, vol. 38, no. 4, pp. 817–824, 2010.

[14] J. J. Zhang, F. Zhou, G. C. Sun, M. D. Xing, and Z. Bao, "High signal-noise-ratio high-resolution wide-swath imaging using two-dimensional intra-pulse beam steering," *J. Xidian Univ.*, vol. 41, no. 4, pp. 6–12, 2014.

[15] F. Zhang, X. Yao, H. Tang, Q. Yin, Y. Hu, and B. Lei, "Multiple mode SAR raw data simulation and parallel acceleration for gaofen-3 mission," *IEEE J. Sel. Topics Appl. Earth Observ. Remote Sens.*, vol. 11, no. 6, pp. 2115–2126, Jun. 2018.

[16] C. Qian, Z. Shao, X. Si, H. Wang, C. Li, and M. Xing, "An antenna beam control method of spaceborne multi-mode imaging SAR based on real-time computing framework," in *Proc. 3rd China Int. SAR Symp.*, 2022, pp. 1–6.

[17] G. Krieger, N. Gebert, and A. Moreira, "Multidimensional waveform encoding: A new digital beamforming technique for synthetic aperture radar remote sensing," *IEEE Trans. Geosci. Remote Sens.*, vol. 46, no. 1, pp. 31–46, Jan. 2008.

[18] G. C. Sun, M. D. Xing, Y. Wang, Y. Wu, and Z. Bao, "Sliding spotlight and TOPS SAR data processing without sub-aperture," *IEEE Geosci. Remote Sens. Lett.*, vol. 8, no. 6, pp. 1036–1040, Nov. 2011.

[19] W. Yang, J. Chen, W. Liu, P. B. Wang, and C. Li, "A modified three-step algorithm for TOPS and sliding spotlight SAR data processing," *IEEE Trans. Geosci. Remote Sens.*, vol. 55, no. 12, pp. 6910–6921, Dec. 2017.

[20] T. Z. Fang, H. Zhang, D. Liang, L. Zhang, and H. T. Fan, "A channel phase error estimation method for multichannel TOPS and multichannel sliding spotlight SAR imaging," *IEEE Geosci. Remote Sens. Lett.*, vol. 19, 2022, Art. no. 4010505.

[21] X. S. Li, G. C. Sun, P. Shao, Y. Wu, and M. D. Xing, "Investigation on multimode SAR imaging based on digital array radar," *J. Radar*, vol. 3, no. 4, pp. 408–489, 2014.

[22] G. Krieger, M. Younis, and S. Huber, "Digital beamforming and MIMO-SAR: Review and new concepts," in *Proc. 9th Eur. Conf. Synthetic Aperture Radar*, 2012, pp. 11–14.

[23] Y. M. Wu, Z. Chen, F. Xu, R. Duan, and C. Jiang, "Multidimensional waveform design for multi-mode and synthetic bandwidth SAR imaging," in *Proc. IEEE CIE Int. Conf. Radar*, 2011, pp. 1259–1262.

[24] C. Diego, S. Matteo, and L. Pierfrancesco, "SAR imaging solution based on azimuth phase coding," in *Proc. 7th Eur. Conf. Synthetic Aperture Radar*, 2008, pp. 57–60.

[25] G. B. Jing, M. D. Xing, J. L. Chen, G. C. Sun, and Z. Bao, "A novel digital beam-forming (DBF) method for multi-modes MIMO-SAR," in *Proc. CIE Int. Conf. Radar*, 2016, pp. 1–5.

[26] F. Zhou, J. Q. Ai, Z. Y. Dong, J. J. Zhang, and M. D. Xing, "A novel MIMO–SAR solution based on azimuth phase coding waveforms and digital beamforming," *Sensors*, vol. 18, no. 10, 2018, Art. no. 3374.

[27] H. B. Wang, Y. Zhang, J. Xu, G. Liao, and C. Zeng, "Study on coding scheme for space-pulse-phase-coding-based high-resolution and wide-swath SAR imaging," *Int. J. Remote Sens.*, vol. 41, no. 18, pp. 7202–7216, 2020.

[28] X. J. Wen, X. L. Qiu, L. Cui, J. Y. Wang, and Q. Chen, "An improved azimuth ambiguity suppression method for SAR based on ambiguity area imaging and detection," *IEEE J. Sel. Topics Appl. Earth Observ. Remote Sens.*, vol. 15, pp. 8155–8169, 2022.

[29] L. M. H. Ulander, H. Hellsten, and G. Stenström, "Synthetic-aperture radar processing using fast factorized back-projection," *IEEE Trans. Aerosp. Electron. Syst.*, vol. 39, no. 3, pp. 760–776, Jul. 2003.

[30] L. Zhang, H. L. Li, Z. J. Qiao, and Z. W. Xu, "A fast BP algorithm with wavenumber spectrum fusion for high-resolution spotlight SAR imaging," *IEEE Geosci. Remote Sens. Lett.*, vol. 11, no. 9, pp. 1460–1464, Sep. 2014.

[31] G. C. Sun et al., "A real-time imaging algorithm based on sub-aperture CS-dechirp for GF3-SAR data," *Sensors*, vol. 18, no. 8, pp. 2562, 2018.

[32] A. Moreira, "Real-time synthetic aperture radar (SAR) processing with a new sub-aperture approach," *IEEE Trans. Geosci. Remote Sens.*, vol. 30, no. 4, pp. 714–722, Apr. 1992.

[33] F. Zhou, J. Yang, G. C. Sun, and J. J. Zhang, "A real-time imaging processing method based on modified RMA with sub-aperture images fusion for spaceborne spotlight SAR," in *Proc. IEEE Int. Geosci. Remote Sens. Symp.*, 2020, pp. 1905–1908.

[34] Y. B. Liu et al., "High-resolution real-time imaging processing for space-borne spotlight SAR with curved orbit via sub-aperture coherent superposition in image domain," *IEEE J. Sel. Topics Appl. Earth Observ. Remote Sens.*, vol. 15, pp. 1992–2003, 2022.

[35] M. Yang and D. Zhu, "An efficient imaging scheme for high-resolution sliding spotlight SAR based on coherent superposition of sub-aperture images," in *Proc. IET Int. Radar Conf.*, 2020, pp. 1082–1085.

[36] Y. S. Li, L. P. Chen, D. An, and D. Feng, "An extracting DEM method based on the sub-apertures difference in CSAR mode," *Int. J. Remote Sens.*, vol. 43, no. 1, pp. 370–391, 2022.

[37] J. J. Zhang, G. C. Sun, M. D. Xing, Z. Bao, and F. Zhou, "An efficient signal reconstruction algorithm for stepped frequency MIMO-SAR in the spotlight and sliding spotlight modes," *Int. J. Antennas Propag.*, vol. 2014, 2014, Art. no. 329340.

[38] Q. S. Wu, W. Jing, M. D. Xing, and Z. Bao, "Wide swath imaging with multidimensional waveform encoding," *J. Xidian Univ.*, vol. 36, no. 5, pp. 801–845, 2009.

[39] Q. S. Wu, M. D. Xing, B. Liu, and Z. Bao, "High azimuth resolution wide swath imaging based on the intra-pulse spotlight SAR," *J. Xidian Univ.*, vol. 37, no. 4, pp. 677–4682, 2010.

[40] F. Zhou, J. Yang, L. Jia, X. M. Yang, and M. D. Xing, "Ultra-high resolution imaging method for distributed small satellite spotlight MIMO-SAR based on sub-aperture image fusion," *Sensors*, vol. 21, no. 5, pp. 1609, 2021.

[41] L. Ma, G. S. Liao, A. F. Liu, Y. L. Jiang, and L. Chen, "Array-error estimation method for multi-channel SAR systems in azimuth," *J. Syst. Eng. Electron.*, vol. 27, no. 4, pp. 815–821, 2016.

[42] Y. J. Kim, G. H. Noh, H. L. Lee, and S. Yu, "Dual-polarized multi-channel 24 GHz radar sensor antenna for high channel-to-channel isolation," *Sensors*, vol. 20, no. 18, 2020, Art. no. 5233.

Fang Zhou (Member, IEEE) was born in Anhui, China. She received the B.S. and Ph.D. degrees in electrical engineering from Xidian University, Xi'an, China, in 2009 and 2014, respectively.

She is currently an Associate Professor with the School of Computer and Information, Hefei University of Technology, Hefei, China. Her research interests include synthetic aperture radar signal processing and correction.

Guoqing Shen was born in Anhui, China, in 1997. He received the B.S. degree in communication engineering from the School of Computer and Information, Anhui Agricultural University, Hefei, China, in 2021. He is currently working toward the master's degree in signal and information processing with the School of Computer and Information, Hefei University of Technology, Hefei, China.

His research interests include MIMO-SAR imaging and multiangle imaging.

Yifan Liu was born in Hebei, China, in 1998. He received the B.S. degree in electronic information science and technology, in 2020, from the School of Computer and Information, Hefei University of Technology, Hefei, China, where he is currently working toward the master's degree in signal and information processing with the School of Computer and Information.

His research interests include MIMO-SAR imaging.

Jing Fang was born in Anhui, China. She received the M.S. degree in pattern recognition and artificial intelligence and Ph.D. degree in photolog from the Hefei Institutes of Physical Science, Chinese Academy of Sciences, Hefei, China, in 2004 and 2009, respectively.

She is currently an Associate Professor with the School of Computer and Information, Hefei University of Technology, Hefei, China. Her research interests include Optical information processing and machine vision.

Jiajia Zhang was born in Anhui, China, in 1986. He received the B.S. and Ph.D. degrees in electrical engineering from Xidian University, Xi'an, China, in 2008 and 2014, respectively.

He is currently a Senior Engineer with the Key Laboratory of Aperture Array and Space Application, East China Research Institute of Electronic Engineering, Hefei, China. His research interests include synthetic aperture radar system.

Mengdao Xing (Fellow, IEEE) received the B.S. degree in information engineering and Ph.D. degree in digital signal processing from Xidian University, Xi'an, Shaanxi, China, in 1997 and 2002, respectively.

He is currently a Professor with the National Laboratory of Radar Signal Processing, Xidian University. He holds the appointment of Dean with the Academy of Advanced Interdisciplinary Research department, Xidian University. He has authored or coauthored more than 200 refereed scientific journal articles. He also has authored or coauthored two books about SAR signal processing. The total citation times of his research are greater than 10 000 (H-index 50). He was rated as Most Cited Chinese Researchers by Elsevier. He has achieved over 50 authorized China patents. His research has been supported by various funding programs, such as, National Science Fund for Distinguished Young Scholars. He has authored or coauthored several Special Issues on *IEEE Geoscience and Remote Sensing Magazine* and IEEE JOURNAL OF SELECTED TOPICS IN APPLIED EARTH OBSERVATIONS AND REMOTE SENSING. His research interests include synthetic aperture radar (SAR), SAR interferometry, inversed SAR, sparse signal processing, and microwave remote sensing.

Dr. Xing serves as the Associate Editor for radar remote sensing of the IEEE TRANSACTIONS ON GEOSCIENCE and *Remote Sensing* and the Editor-in-Chief of MDPI *Sensors*.